

# Detection of emission lines from $z \sim 3$ DLAs towards the QSO J2358+0149<sup>\*</sup>

Raghunathan Srianand<sup>1</sup>†, Tanvir Hussain<sup>1</sup>, Pasquier Noterdaeme<sup>2</sup>, Patrick Petitjean<sup>2</sup>, Thomas Krühler<sup>3,4</sup>, Jure Japelj<sup>5,6</sup>, Isabelle Pâris<sup>6</sup> & Nobunari Kashikawa<sup>7</sup>

<sup>1</sup> IUCAA, Postbag 4, Ganeshkhind, Pune 411007, India

<sup>2</sup> Institut d’Astrophysique de Paris, CNRS-UPMC, UMR 7095, 98bis bd Arago, 75014, Paris, France

<sup>3</sup> European Southern Observatory, Alonso de Córdova 3107, Vitacura, Casilla 19001, Santiago 19, Chile

<sup>4</sup> Max-Planck-Institut für extraterrestrische Physik, Giessenbachstraße, 85748 Garching, Germany

<sup>5</sup> Faculty of Mathematics and Physics, University of Ljubljana, Jadranska ulica 19, 1000 Ljubljana, Slovenia

<sup>6</sup> INAF-Osservatorio Astronomico di Trieste, via G. B. Tiepolo 11, 34131 Trieste, Italy

<sup>7</sup> Optical and Infrared Astronomy Division, National Astronomical Observatory, Mitaka, Tokyo 181-8588, Japan

Accepted 2016 April 20. Received 2016 April 20; in original form 2015 October 13

## ABSTRACT

Using VLT/X-shooter we searched for emission line galaxies associated to four damped Lyman- $\alpha$  systems (DLAs) and one sub-DLA at  $2.73 \leq z \leq 3.25$  towards QSO J2358+0149. We detect [O III] emission from a “low-cool” DLA at  $z_{\text{abs}} = 2.9791$  (having  $\log N(\text{H I}) = 21.69 \pm 0.10$ ,  $[\text{Zn}/\text{H}] = -1.83 \pm 0.18$ ) at an impact parameter of,  $\rho \sim 12$  kpc. The associated galaxy is compact with a dynamical mass of  $(1 - 6) \times 10^9 M_{\odot}$ , very high excitation ( $[\text{O III}]/[\text{O II}]$  and  $[\text{O III}]/[\text{H}\beta]$  both greater than 10),  $12+[\text{O}/\text{H}] \leq 8.5$  and moderate star formation rate ( $\text{SFR} \leq 2 M_{\odot} \text{ yr}^{-1}$ ). Such properties are typically seen in the low- $z$  extreme blue compact dwarf galaxies. The kinematics of the gas is inconsistent with that of an extended disk and the gas is part of either a large scale wind or cold accretion. We detect Ly $\alpha$  emission from the  $z_{\text{abs}} = 3.2477$  DLA (having  $\log N(\text{H I}) = 21.12 \pm 0.10$  and  $[\text{Zn}/\text{H}] = -0.97 \pm 0.13$ ). The Ly $\alpha$  emission is redshifted with respect to the metal absorption lines by  $320 \text{ km s}^{-1}$ , consistent with the location of the red hump expected in radiative transport models. We derive  $\text{SFR} \sim 0.2 - 1.7 M_{\odot} \text{ yr}^{-1}$  and Ly $\alpha$  escape fraction of  $\geq 10$  per cent. No other emission line is detected from this system. Because the DLA has a small velocity separation from the quasar ( $\sim 500 \text{ km s}^{-1}$ ) and the DLA emission is located within a small projected distance ( $\rho < 5$  kpc), we also explore the possibility that the Ly $\alpha$  emission is being induced by the QSO itself. QSO induced Ly $\alpha$  fluorescence is possible if the DLA is within a physical separation of 340 kpc to the QSO. Detection of stellar continuum light and/or the oxygen emission lines would disfavor this possibility. We do not detect any emission line from the remaining three systems.

**Key words:** quasars: active – quasars: absorption lines – quasars: individual: SDSS J235854.4+014955.5 – ISM: lines and bands

## 1 INTRODUCTION

Damped Ly $\alpha$  systems (DLAs with  $N(\text{H I}) \geq 2 \times 10^{20} \text{ cm}^{-2}$ ), seen in the spectra of bright background sources like QSOs, in principle trace galaxies based on their projected H I gas cross-section and thereby providing a luminosity independent probe of high- $z$  galaxies (see Wolfe et al. 2005). Thanks to large spectroscopic

surveys, we now have a very good statistical sample of DLAs in the redshift range  $2 \leq z \leq 4$  (Prochaska et al. 2005; Noterdaeme et al. 2009, 2012b). DLAs at these redshifts contain  $\sim 80\%$  of the neutral gas and the cosmic density of H I gas in DLAs (i.e.  $\Omega_{\text{H I}}$ ) shows an increasing trend at  $2 \leq z \leq 4$ , while within statistical uncertainties evolving very mildly at  $z \leq 2$ . At  $z > 4$  the data does not show a clear trend either due to small number statistics or, especially when spectral resolution is low, from systematics due to blending with Ly $\alpha$  forest (Péroux et al. 2003; Guimarães et al. 2009; Songaila & Cowie 2010; Zafar et al. 2013; Crighton et al. 2015).

Based on novel broad-band color selection and narrow-band imaging techniques, galaxies are detected up to  $z \sim 10$  and the star

<sup>\*</sup> Based on observations carried out at the European Southern Observatory (ESO) under programme ID 293.A-5020(A) (P.I. Noterdaeme) using X-Shooter spectrograph located on Unit Telescope 3 (UT3, Melipal) of the Very Large Telescope (VLT) at the Paranal Observatory, Chile.

† E-mail: anand@iucaa.in

formation rate density of galaxies is mapped up to  $z \sim 10$  (see [Madau & Dickinson 2014](#)). There is a strong increase in the UV luminosity density by 0.8 to 1 dex between  $z = 0$  and  $z \sim 2$  followed by a decrease towards higher  $z$  for  $z \geq 3$ . High spatial resolution deep imaging studies show, galaxies at  $z \sim 3$  have sizes typically a factor 3 smaller compared to their local counterparts of similar luminosity (e.g., [Trujillo et al. 2006](#)).

The observed number density of DLAs requires that the total HI cross-section must be much larger than the optical extent of galaxies currently detected in emission, indicating wide spread of HI around these galaxies (either in extended discs or in flows) or that a significant contribution to the gas cross-section comes from the population of faint galaxies below the detection limit of large surveys. It is believed that the redshift evolution of the star formation rate density in the universe is driven by cold inflows (see for example, [Kereš et al. 2005](#); [Erb et al. 2006](#); [Ocvirk et al. 2008](#); [Dekel et al. 2009](#)) and probably controlled by the large scale outflows that are ubiquitously found among the high redshift Lyman Break Galaxies (LBGs, [Pettini & Bowen 2001](#); [Shapley et al. 2003](#); [Veilleux et al. 2005](#)). These processes may control the physical conditions, chemical composition and kinematics of the extended gas distribution around galaxies (the so called circumgalactic medium) that are probed by absorption line studies.

Purely based on the high resolution spectroscopic studies of DLAs we know that: (i) at a given  $z$ , the average metallicity of DLAs is typically less than those inferred for galaxies from their nebular emission, (ii) metallicity in DLAs shows clear redshift evolution but with a slope shallower than what one would have expected purely based on the galaxy evolution ([Som et al. 2013](#); [Rafelski et al. 2014](#)) (iii) the volume filling factor of cold gas (inferred through tracers like  $H_2$  and 21-cm absorption) is lower than that seen in the local interstellar medium (ISM, [Petitjean et al. 2000](#); [Ledoux et al. 2003](#); [Noterdaeme et al. 2008](#); [Srianand et al. 2012](#); [Kanekar et al. 2014](#)) and (iv) DLAs show clear correlation between the velocity width of the low-ion absorption and the metallicity akin to the mass-metallicity relation seen in galaxies ([Ledoux et al. 2006](#)). [Møller et al. \(2013\)](#) explained the slow metallicity evolution as a consequence of the lack of strong evolution in the zero-point of the mass-metallicity relation of high- $z$  DLA galaxies. [Wolfe et al. \(2008\)](#) based on the cooling rate derived using  $C\text{II}^*$  absorption suggested the existence of “low-cool” and “high-cool” population of DLAs. They argued that both populations need local sources to satisfy the heating requirements (see however, [Srianand et al. 2005](#)). The rare detections of faint, extended objects in the Hubble Ultra Deep Field is incompatible with all heating coming from in situ star formation in “high-cool” DLAs and suggests that they may be originating from extended regions of LBGs ([Wolfe & Chen 2006](#)). All this, while suggesting that the DLAs are somehow related to the star forming regions, also suggest that they need not always be related to the gas in the stellar disk of galaxies.

Therefore, identifying galaxies and correlating galaxy properties derived using continuum and nebular emission lines to the properties of the associated DLAs derived from the high resolution spectra of QSO is very important. There have been several attempts to detected galaxies associated to high- $z$  DLAs. However, searches aimed at directly detecting associated galaxies either in the continuum emission or in the nebular line emission have mostly resulted in non-detections ([Bunker et al. 1999](#); [Kulkarni et al. 2000](#); [Lowenthal et al. 1995](#); [Christensen et al. 2009](#); [Fumagalli et al. 2015](#), as well as several unpublished works.)

with very few cases being spectroscopically confirmed by the detection of  $\text{Ly}\alpha$  and/or other emission lines ([Møller et al. 2002, 2004](#); [Fynbo et al. 2010](#); [Noterdaeme et al. 2012a](#); [Fynbo et al. 2013](#); [Krogager et al. 2013](#); [Bouché et al. 2013](#); [Hartoog et al. 2015](#)). These systems are used to obtain different correlations between properties derived from absorption lines towards quasars and emission lines from the associated galaxies. [Krogager et al. \(2012\)](#) found a possible anti-correlation between  $N(\text{HI})$  and impact parameter (see their Fig. 3) similar to the one seen at low- $z$  based on HI emission maps (see Fig. 15 of [Zwaan et al. 2005](#)). A possible correlation is also seen between the metallicity of the DLAs and the impact parameter. These correlations are shown to be consistent with a scenario where the metallicity-size relation is driven by starburst induced feed back processes. [Christensen et al. \(2014\)](#) measured stellar masses of these DLA host galaxies. These are found to be consistent with the expected values based on mass-metallicity relations. As these interesting correlations are based on a handful of known systems studied in detail, it is important to increase the number of galaxies associated with DLAs.

Information on average star formation in DLA galaxies can in principle be derived using  $\text{Ly}\alpha$  stacking methods ([Rahmani et al. 2010](#); [Noterdaeme et al. 2014](#)). However, complexities involved in the radiative transport of  $\text{Ly}\alpha$  photons may hinder our interpretation in the absence of independent escape fraction measurements.

One possible way to enhance the efficiency of searching for DLA galaxies is to target QSO sightlines with multiple DLAs in the optical near-IR regions. By scanning the full sample of QSO spectra from the SDSS-III Baryonic Oscillation Spectroscopic Survey (BOSS) - Data Release 13 ([Pâris et al. 2014](#)) we have identified a QSO sightline having 5 systems with  $\text{Ly}\alpha$  showing damping wings along the line of sight. In this paper, we present analysis of these five intervening DLA systems at  $z_{\text{abs}} = 2.7377, 2.9791, 3.1095, 3.1333$  and  $3.2477$  towards the SDSS J235854.4+014955.5 (hereafter refer to as J2358+0149). In particular, we report detection of  $[\text{O III}]$  and  $\text{Ly}\alpha$  emission associated with DLAs at  $z_{\text{abs}} = 2.9791$  and  $3.2477$  respectively. In Section 2, we provide details of the VLT/X-shooter observations, data reduction and systemic redshift measurements of the QSO. In Section 3 we present the analysis of the intervening absorption systems and a discussion on chemical abundances and dust depletions. We discuss, in Section 4 and 5, the emission properties of the DLA galaxies. The summary and conclusions are presented in Section 6. In this paper we use a standard  $\Lambda$ CDM cosmology with  $\Omega_{\Lambda} = 0.73$ ,  $\Omega_m = 0.27$ , and  $H_0 = 70 \text{ km s}^{-1} \text{ Mpc}^{-1}$ .

## 2 DATA AND DETAILS OF X-SHOOTER OBSERVATIONS:

Spectra of J2358+0149 were obtained with X-shooter ([Vernet et al. 2011](#)) at the European Southern Observatory (ESO) Very Large Telescope (VLT) in service mode under Director’s Discretionary Time (PI: Noterdaeme). Our observations consist of 5 observation blocks (OBs) for a total science exposure time of 14500 s in the ultra-violet-blue (UVB), 14000 s in the visible (VIS) and 14400 s in the near-infrared (NIR) arm respectively. Each OB was performed using one nodding cycle (AB) with a nod throw of 4". NIR exposures were split into 480 s DITs (detector integration times). In order to be able to use the triangulation technique to get the galaxy impact parameter with respect to the QSO line of sight using emission line centroids, we have arranged the 5 OBs in the following way: two at position angles of  $0^\circ$  (North

**Table 1.** Log of X-shooter observations of J2358+0149<sup>†</sup>

PA (deg)	Observing date dd/mm/year	DIMM seeing (arcsec)	Air mass	Exposure time(s)		
				UVB	VIS	NIR
0	02-07-2014	0.9	1.14	2×2900	2×2800	2×2880
+60	04-08-2014	1.0	1.20	2×2900	2×2800	2×2880
-60	01-07-2014	0.8	1.20	1×2900	1×2800	1×2880

<sup>†</sup> Slit widths of 1.2, 0.8 and 1.3 arcsec were used for UVB, VIS and NIR spectrographs of the X-shooter, respectively.

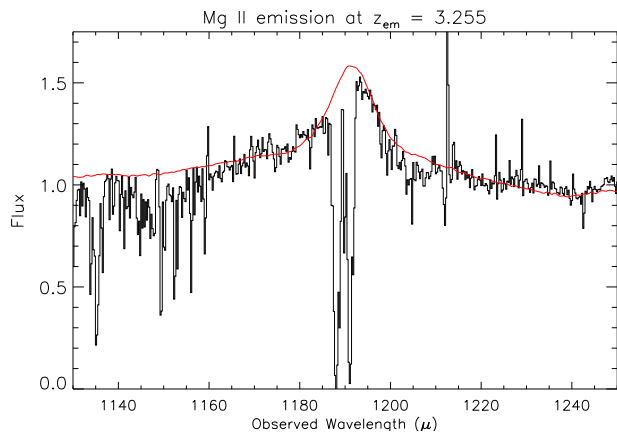


**Figure 1.** The Mg II broad emission line detected in the near-IR spectrum of J2358+0149. Composite QSO spectrum redshift to  $z_{em} = 3.255$  is overlaid for comparison.

of East), two with PA=60° and one at position -60°. Apart from the differences in the position angle, other settings used in all OBs were identical. The observations were performed under good seeing (0.8-1.0 arcsec) conditions. Detailed observational log is provided in Table 1.

We reduced the X-shooter spectra using the ESO pipeline (version 2.5.2; Goldoni et al. 2006). We performed flat-fielding, order tracing, rectification and initial wavelength and flux calibration. For sky-subtraction, stacking of individual exposures, bad-pixel masking and cosmic ray rejection, we applied our own software and followed the procedure described in detail in Krühler et al. (2015). Very briefly, we combined the individual, sky-subtracted exposures taken in a single position angle with a weighted average, where the weight function was derived from the signal-to-noise ratio of the QSO spectrum. Bad pixel and cosmic rays were detected using a Laplacian edge detection filter and masked in the final stack. Error spectra, initially derived through the ESO pipeline, were propagated accordingly.

The X-shooter spectrum covers the wavelength range from 300 nm to 2.5 μm at the intermediate spectral resolution ( $R \sim 6000$  to 7000), thereby allowing an accurate measurement of the systemic redshift of the QSO and simultaneous search for the Ly $\alpha$  emission in the blue and standard optical nebular lines like [O II], [O III] and H $\beta$  in the NIR from the  $z \sim 3$  DLAs.

In the optical UV spectrum of the QSO the Ly $\alpha$  + N V emission lines are severely absorbed by the associated DLA absorption at  $z_{abs} = 3.2477$ . The [C III], Si IV and C IV emission lines are also weak, broad and asymmetric compared to that of the QSO composite spectrum. Based on C IV and Si IV emission lines we get the QSO redshift of  $z_{em} = 3.235$ . We also do not detect strong [O III] emission from the QSO though there is a weak feature coinciding with the H $\beta$  emission. The only prominent

broad emission line that is symmetric is Mg II line that we detect in the near-IR spectrum (see Fig 1). We fit the Mg II profile with a Gaussian and estimated the emission redshift to be  $z_{em} = 3.255 \pm 0.001$ . In what follows, we use  $z_{em} = 3.255$  for all practical purposes.

### 3 BRIEF DESCRIPTION OF METALS IN INDIVIDUAL SYSTEMS

Along the J2358+0149 sightline, we detect five absorption systems with Ly $\alpha$  absorption showing damping wings : one sub-DLA (at  $z_{abs} = 2.73773$ ) and four DLAs (at  $z_{abs} = 2.97919$ , 3.10956, 3.13333 and 3.24772). We estimate the column densities of H I and metal ions using the Voigt profile fitting code VPFIT<sup>1</sup> version 10.0. The Voigt profile fits to the Ly $\alpha$  absorption lines are shown in Fig 2. In the case of metal lines, while fitting the profiles<sup>2</sup> we keep the  $z$  and  $b$ -parameter for each component to be same for all the species (i.e. species are assumed to be tied to each other and the absorption profile is dominated by non-thermal motions). Due to the intermediate resolution of the X-shooter spectrum, hidden saturation in the narrow lines can hinder our metallicity measurements. Therefore, as far as possible we discuss the metallicities of species that were measured using several lines having a wide range of oscillator strengths. In particular this is true for Fe II and Si II. Voigt profile fits overlaid on the data for all the 5 systems are presented in the Appendix (see Fig. A1-A5). We also summarize the results of Voigt profile fitting of individual components in tables given in the Appendix (see tables A1-A5). The set of transitions used to derive these fits are provided when we discuss individual systems below. The total column densities of different species obtained are summarized in Table 2. The metallicity<sup>3</sup> of individual ions detected (without applying ionization corrections) in these five systems are summarized in Table 3. We provide a short summary of each system in this section. For all discussion on metallicity we use solar relative abundances of the metals taken from Asplund et al. (2009).

#### 3.1 The sub-DLA at $z_{abs} = 2.7377$

The Voigt profile fit to the damped Ly $\alpha$  absorption gives  $\log N(\text{H I}) = 20.07 \pm 0.05$  (see Fig. 2). In addition to the Ly $\alpha$ , absorption

<sup>1</sup> <http://www.ast.cam.ac.uk/~rfc/vpfit.html>

<sup>2</sup> As the seeing during our observations was better than the slit width used, the actual resolution achieved is slightly better than the normal value. Therefore, we adjusted the instrumental profile by fitting the narrow telluric absorption lines. The measured resolution is  $R \approx 9700$  and 6000 in the visible and UVB respectively. We use these values to generate instrumental profiles while fitting the absorption lines. Note this effect is not important in the case of extended line emission from galaxies.

<sup>3</sup>  $[Z/H] \equiv \log(Z/H)_{obs} - \log(Z/H)_{\odot}$

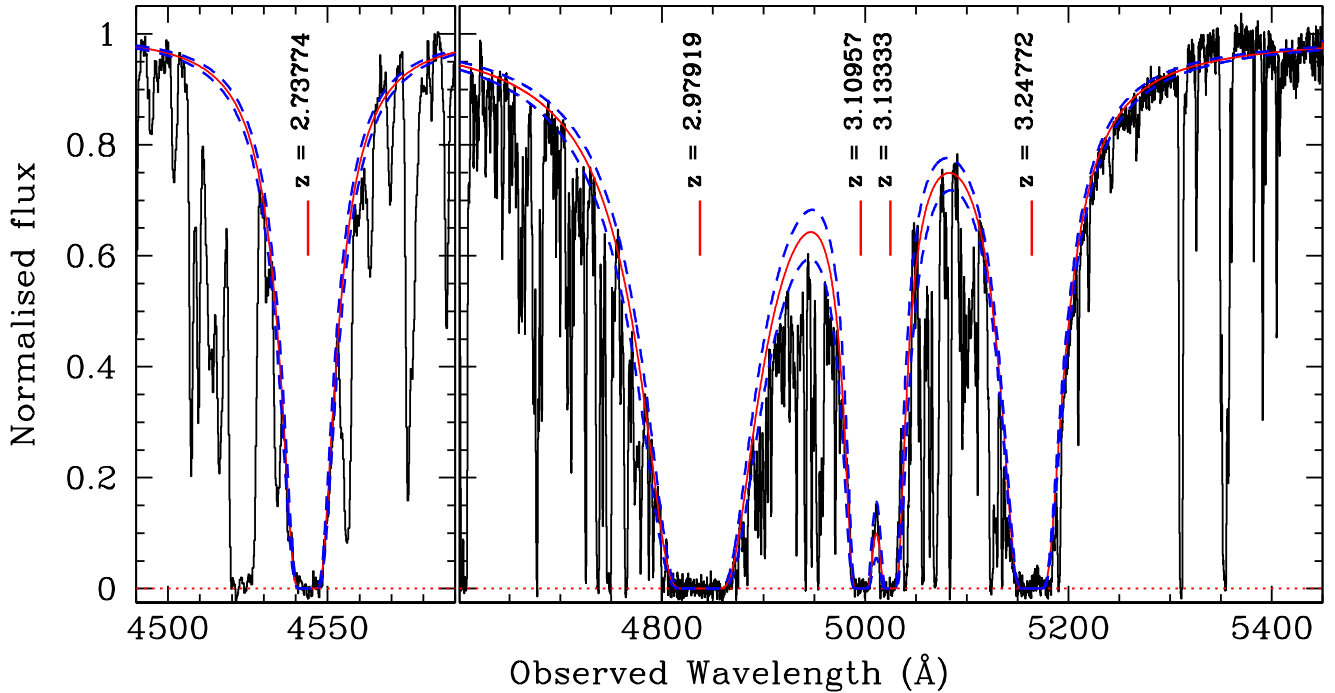


**Figure 2.** *Left panel:* Voigt profile fits to the Ly $\alpha$  absorption from the sub-DLA at  $z_{\text{abs}}=2.73774$ . *Right panel:* Simultaneous Voigt profile fit to Ly $\alpha$  absorption from four DLAs at  $z_{\text{abs}}=2.97919, 3.10957, 3.13333$  and  $3.24772$ . Dashed profiles show the  $1\sigma$  range.

**Table 2.** Total column densities of metals and neutral hydrogen in DLAs

$z_{\text{abs}}$	$\log N$ ( $\text{cm}^{-2}$ )						
	H I	Si II <sup>1</sup>	S II	Fe II	Ni II	Cr II	Zn II
2.73774	$20.07 \pm 0.05$	$13.90 \pm 0.14$	$< 13.73 \pm 0.35$	$13.52 \pm 0.33$	–	–	–
2.97919	$21.69 \pm 0.10$	$15.49 \pm 0.24$	–	$15.21 \pm 0.15$	$13.70 \pm 0.31$	$13.16 \pm 0.21$	$12.42 \pm 0.15$
3.10957	$20.45 \pm 0.10$	$14.66 \pm 0.09$	–	$14.37 \pm 0.11$	–	–	–
3.13333	$20.33 \pm 0.10$	$14.67 \pm 0.45$	–	$13.82 \pm 0.16$	–	–	–
3.24772	$21.12 \pm 0.10$	$15.68 \pm 0.12$	$15.08 \pm 0.08$	$15.12 \pm 0.12$	$13.64 \pm 0.17$	$13.39 \pm 0.09$	$12.71 \pm 0.09$

<sup>1</sup> The quoted column density can be affected by the presence of hidden saturation components if they have  $b < 4 \text{ km s}^{-1}$ . See text.

**Table 3.** Metal abundances in DLAs

$z_{\text{abs}}$	[Si/H]	[S/H]	[Fe/H]	[Ni/H]	[Cr/H]	[Zn/H]
2.73774	$-1.68 \pm 0.14$	$< -1.81$	$-2.05 \pm 0.33$	–	–	–
2.97919	$-1.71 \pm 0.26$	–	$-1.98 \pm 0.18$	$-2.21 \pm 0.32$	$-2.17 \pm 0.23$	$-1.83 \pm 0.18$
3.10957	$-1.30 \pm 0.13$	–	$-1.58 \pm 0.15$	–	–	–
3.13333	$-1.17 \pm 0.46$	–	$-2.01 \pm 0.19$	–	–	–
3.24772	$-0.95 \pm 0.15$	$-1.16 \pm 0.13$	$-1.50 \pm 0.16$	$-1.70 \pm 0.20$	$-1.37 \pm 0.13$	$-0.97 \pm 0.13$

lines from Si II, S II, Fe II and Mg II lines are detected. At the resolution of our spectrum these lines are unresolved. We measure rest equivalent width ( $W_r$ ) of 0.50 and 0.40 Å for the Mg II doublets. The expected position of C II absorption falls in the Ly $\alpha$  absorption of the  $z_{\text{abs}}=2.9791$  system. Therefore, we could not have a handle on the gas cooling rate for this system. To get a better constraint on the column density measurements, we perform Voigt profile fits of Si II  $\lambda 1526$  and Fe II  $\lambda\lambda 2382, 2374, 2344$ . The best fit Voigt

profiles for this system is shown in Fig. A1 and measured column densities are shown in Table. 2. A  $3\sigma$  upper limit to the column density is measured for blended S II transitions in this system. The metallicity of the gas based on Si II absorption is [Si/H] =  $-1.68 \pm 0.14$ . The measured upper limit on sulphur metallicity based on S II (i.e.  $\leq -1.81$ ) are consistent with this metallicity (see Table 3). Based on the observed Fe II column density we derive [Fe/H] =  $-2.05 \pm 0.33$ . Even though the mean metallicity of Fe

suggests a possible under abundance, the errors are too large to draw any firm conclusion. We do not detect  $H_2$  from this system. Given the low metallicity and low  $N(H\text{I})$  measured in this system, non-detection of  $H_2$  is not at all surprising (Petitjean et al. 2006). This system does not show a strong C IV absorption (with  $W_r(\text{C IV } \lambda 1548) \sim 0.05 \text{ \AA}$ ). However, it is interesting to note that the nearest Ly $\alpha$  absorption system with a velocity separation of  $\sim 950 \text{ km s}^{-1}$  (i.e. at  $z_{\text{abs}} = 2.7259$ , the line seen at  $\sim 4530 \text{ \AA}$  in Fig. 2) shows a strong C IV (with  $W_r(\text{C IV } \lambda 1548) \sim 0.34 \text{ \AA}$ ) and Si IV absorption. In our 2D spectrum we do not detect any associated emission line galaxy at all three position angles within the impact parameter probed (i.e.  $\leq 15 \text{ kpc}$ ).

### 3.2 The DLA at $z_{\text{abs}} = 2.9791$

This is the system with the highest H I column density along the line of sight to J2358+0149. The Voigt profile fit to the Ly $\alpha$  line gives  $\log N(\text{H I}) = 21.69 \pm 0.10$  (see Fig. 2). This is close to the limiting column density ( $\log N(\text{H I}) = 21.7$ ) used by Noterdaeme et al. (2014) to define extremely strong DLAs (ESDLAs). In this system, absorption lines of C II, Si II, Cr II, Fe II, Ni II and Zn II along with C II\* are detected. Even at the spectral resolution of the X-shooter most of the absorption lines are saturated. In the NIR spectrum we detect very strong Mg II (with  $W_r \sim 2.6 \text{ \AA}$  and  $2.2 \text{ \AA}$  for the doublet) Fe II  $\lambda 2600$  (with  $W_r \sim 1.9 \text{ \AA}$ ) and Mg I (with  $W_r \sim 1.7 \text{ \AA}$ ) lines. Thus purely based on Mg II absorption strength this system is in the lower end of “ultra-strong” Mg II systems. Such absorbers show very large velocity spread and are thought to be associated either with supernova driven winds (see for example, Nestor et al. 2011) or cold gas embedded in intragroup media (Gauthier 2013). Using the JHU-SDSS catalog (Zhu & Ménard 2013) of Mg II absorbers we find that only 0.5% of the Mg II absorbers at  $z_{\text{abs}} \geq 2.0$  have such large equivalent widths for Mg II and Fe II. Thus based on observed  $N(\text{H I})$  and equivalent widths of Mg II and Fe II the present system seems to be a rare system among the QSO absorption line systems.

As expected the absorption line from singly ionized species spread over  $\sim 240 \text{ km s}^{-1}$  whereas C IV absorption spread over  $400 \text{ km s}^{-1}$  (see Fig. 5). Using the definition of Ledoux et al. (2006), we measure  $\Delta v_{90}^4$  of 168, 141 and  $144 \text{ km s}^{-1}$  for Fe II  $\lambda 1608$ , Si II  $\lambda 1808$  and C IV  $\lambda 1548$  respectively. Only  $\sim 19\%$  of high- $z$  DLAs show such a large velocity spread of low ion absorption lines (see Fig. 9 of Noterdaeme et al. 2008). The velocity spread similar to the one we see for C IV is also very rare in DLAs (see Fig. 2 of Fox et al. 2007) and in intervening Ly $\alpha$  forest absorbers (see Fig. 11 of Muzahid et al. 2012). We will discuss the implications of the large velocity width in detail in Section 4.

The Voigt profile fits to the absorption lines were performed using Si II  $\lambda\lambda 1526, 1808$ , Fe II  $\lambda\lambda 1608, 2249, 2260$ , Cr II  $\lambda 2062$ , Ni II  $\lambda 1709$ , Zn II  $\lambda 2026$  and C II\*  $\lambda 1335.7$  simultaneously with five components. The contribution of the blends Cr II  $\lambda 2026$  and Mg I  $\lambda 2026$  in Zn II  $\lambda 2026$  has to be taken care of while fitting. As we do not have independent constraints on Mg I column densities, uncertainties in the derived Zn II column density may be higher than the statistical error we quote. The derived parameters are presented in Table 2 and the fit is shown in Fig. A2. We measure  $[\text{Zn}/\text{H}] = -1.83 \pm 0.18$  and  $[\text{Si}/\text{H}] = -1.71 \pm 0.26$ . This is

<sup>4</sup> Using the moderate resolution spectrum can bias the derived  $\Delta v_{90}$  values. However, for the spectral resolution of the X-shooter, this effect is expected to be small for the  $\Delta v_{90}$  value we find here (see Fig. 1 of Arabsalmani et al. 2015).

consistent with a low metallicity gas without relative enhancement of  $\alpha$ -elements with respect to the Fe co-production elements. As can be seen from Fig. A2, the absorption profile is well fitted with 5 components with a reduced  $\chi^2_{\nu} \sim 1$ . However, from Table A2 we notice that the main component has a large  $b$ -value. In order to check the possible hidden narrow saturated component in this velocity range, we fitted the absorption profile by fixing the  $b$  parameter in the range  $3\text{--}8 \text{ km s}^{-1}$  as typically derived for metal lines observed at high-resolution. Values lower than this are usually associated with  $H_2$  components (Ledoux et al. 2003; Srianand et al. 2005). The derived column densities are consistent (i.e. at most 0.1 dex higher) with our best fit values in the case of Cr II, Zn II, Fe II and Ni II as we have good constraints from weak lines that have residual fluxes consistent with non-saturation even at these  $b$ -values. However, in the case of Si II for  $b = 3 \text{ km s}^{-1}$  we could accommodate a factor of two higher column density in a hidden saturated component compared to our best fitted value. Therefore, our Si II absorption is susceptible to undetected hidden saturation and high resolution spectrum is needed to get an accurate column density.

The dust content in this absorber can be determined from the depletion factors of metals detected compared to zinc:  $[\text{Cr}/\text{Zn}] = -0.34 \pm 0.29$ ,  $[\text{Fe}/\text{Zn}] = -0.15 \pm 0.25$  and  $[\text{Ni}/\text{Zn}] = -0.38 \pm 0.37$ . The small depletion seen in this very high H I column density absorber is consistent with the lack of strong reddening signatures in the QSO continuum. We do not detect the absorption from C I, Ti II, Na I and Ca II. The expected position of fine-structure lines of O I falls in the red wing of the DLA at  $z_{\text{abs}} = 3.2477$ . We do not detect fine-structure lines of Si II also. We differ a detailed discussions on C II\* cooling rate to Section 4.

It has been suggested that  $H_2$  may be more frequently detected in ESDLAs compared to the normal DLAs (see Noterdaeme et al. 2015a,b). We do not detect  $H_2$  in any of the Voigt profile component of the low ions. We place a  $3\sigma$  upper limit on  $\log N(\text{H}_2, J=0) \leq 15.54$  ( $3\sigma$ ) and for  $\log N(\text{H}_2, J=1) \leq 15.70$  ( $3\sigma$ ) for a line having a typical width of the narrowest line detected in the Ly $\alpha$  forest. We detect an associated galaxy through a strong [O III] emission line. While the BOSS spectrum of the QSO does show an emission feature in the middle of the Ly $\alpha$  absorption we do not detect any Ly $\alpha$  emission in our X-shooter spectrum. Detailed analysis of the galaxy is presented in Section 4.

### 3.3 The DLA at $z_{\text{abs}} = 3.1095$

We measure  $\log N(\text{H I}) = 20.45 \pm 0.10$  for this system. At the X-shooter’s resolution the absorption is mostly concentrated in one component. Absorption from Ar I, N I, O I, C II, Si II, Fe II, Mg II and Mg I are observed in this system. From the NIR spectrum we measure the equivalent widths of Mg II ( $W_r \sim 1.00$  and  $0.88 \text{ \AA}$  for the doublet), Fe II  $\lambda 2600$  ( $W_r \sim 0.58 \text{ \AA}$ ) and Mg I ( $W_r \sim 0.18 \text{ \AA}$ ). We performed Voigt profile fits with two components for N I  $\lambda 1199.5$ , O I  $\lambda\lambda 971, 976, 1039$ , Ar I  $\lambda 1048$ , C II  $\lambda 1334$ , Si II  $\lambda\lambda 1526, 1808$  and Fe II  $\lambda\lambda 1608, 2344, 2374$  transitions. It is possible that our column density estimations are affected by unresolved saturation in the strong resonance transitions like C II. The best fit Voigt profile to the ions is shown in Fig. A3. We derive  $[\text{Si}/\text{H}] = -1.30 \pm 0.13$ ,  $[\text{O}/\text{H}] = -1.87 \pm 0.20$ ,  $[\text{N}/\text{H}] = -2.8 \pm 0.14$ ,  $[\text{Ar}/\text{H}] = -1.61 \pm 0.48$  and  $[\text{Fe}/\text{H}] = -1.58 \pm 0.15$ . The large variations in the metallicity measurements may be a consequence of hidden line saturation (the main component is narrow and requires low  $b$ -value as can be seen in Table A3) and one needs to be cautious in interpreting them. The metallicity measurements

are consistent with very little or no depletion of Fe. As typically seen in other DLAs we also notice  $[N/O]$  being much below the primary line (see, [Petitjean et al. 2008](#); [Cooke et al. 2011](#); [Dutta et al. 2014](#)). The measured abundance pattern makes this system an interesting target for metallicity measurements with high resolution spectroscopy. We do not detect any emission line galaxy associated to this DLA.

### 3.4 The DLA at $z_{\text{abs}} = 3.1333$

The  $\log N(\text{H I}) = 20.33 \pm 0.10$  measured in this system just about satisfies the definition of a DLA. Absorption from C II, Si II, Fe II and O I are observed in this system. The Mg II ( $W_r \sim 0.49$  and  $0.44 \text{ \AA}$  for the doublet) and Fe II  $\lambda 2600$  ( $W_r \sim 0.27 \text{ \AA}$ ) lines are relatively weak compared to the other systems. The column density and  $b$ -parameter measurements of the observed ions are derived from C II  $\lambda 1036$ , Si II  $\lambda \lambda 1526, 1260$ , Fe II  $\lambda \lambda \lambda 2382, 2374, 2344$  and O I  $\lambda 1039$ . The Voigt profile fit to the metals and measured column densities are shown in Fig. A4 and Table 2. The derived  $[\text{Si}/\text{H}] = -1.17 \pm 0.46$  is higher than that of the other DLAs discussed above. We also find  $[\text{Fe}/\text{Si}] = -0.82 \pm 0.50$ . As column densities of Fe II and Si II were obtained using several transitions, this low value of Fe could reflect dust depletion. Due to the low measured  $N(\text{H I})$  we expect this absorber to produce little extinction even if there is dust depletion at the level inferred above. Like the  $z_{\text{abs}} = 3.1095$  system the measured O I column density (i.e.  $\log N(\text{O I}) = 14.93 \pm 0.26$ ) suggests a lower  $[\text{O}/\text{H}] = -2.09 \pm 0.28$  compared to that inferred from the Si measurements. As in the case of the previous system the  $b$ -value for the main component is low (see Table A4) and hidden saturation could affect our metallicity measurement, it will be interesting to measure these abundances with high resolution spectra.

### 3.5 The DLA at $z_{\text{abs}} = 3.2477$

The measured  $z_{\text{abs}}$  of this DLA is very close to the QSO redshift, and the measured velocity,  $v = -515 \text{ km s}^{-1}$ , with respect to the QSO is consistent with the system being a proximate DLA (pDLA, [Ellison et al. 2010](#)). We measure  $\log N(\text{H I}) = 21.12 \pm 0.10$  by fitting the DLA profile. In this system, we detect absorption from C II, S II, Si II, Fe II, Mg II, Mg I, Cr II, Ni II and Zn II. The equivalent width of Mg II absorption ( $W_r \sim 3.8$  and  $4.0 \text{ \AA}$  for the doublet) is much higher than what we have seen for the  $z_{\text{abs}} = 2.9791$  DLA. However Mg I absorption is relatively weaker (i.e.  $W_r(\text{Mg I}) \sim 0.27 \text{ \AA}$ ) compared to that measured in the other systems. This may imply an extended velocity structure in the present system compared to the  $z_{\text{abs}} = 2.9791$  DLA.

Absorption profiles of strong low-ion transitions like Si II  $\lambda 1526$  and Al II  $\lambda 1670$  spread over  $\sim 500 \text{ km s}^{-1}$ , while those of relatively weak low-ion transitions like Fe II  $\lambda 1608$  spread over  $250 \text{ km s}^{-1}$  (see Fig. 7) has  $\Delta v_{90} = 149 \text{ km s}^{-1}$ . Unlike in the case of the  $z_{\text{abs}} = 2.9791$  DLA, the high ionization phase probed by the C IV absorption is not wider than that of the low-ions. However, the C IV absorption profile is distinctly different from those of the low-ions and spread over  $\sim 250 \text{ km s}^{-1}$ . Despite the pDLA being very close to the QSO we do not detect N V or O VI absorption associated to the C IV absorption (as often seen in the associated absorbers in [Petitjean et al. 1994](#)).

Detection of absorption from the excited fine-structure levels of C II, Si II and O I, in the associated absorption systems, can be used to infer the distance of the absorber from the QSO (see for example, [Srianand & Petitjean 2000](#); [Fathivavsari et al.](#)

[2015](#)). Due to the large velocity spread, C II\*  $\lambda 1335$  from the strong components are blended with C II  $\lambda 1334$  from the velocity components in the red. Similarly, the expected wavelength range of O I\*  $\lambda 1304$  and O II\*  $\lambda 1306$  absorption falls with the profile of Si II  $\lambda 1304$  absorption. High resolution spectra are needed to measure the column densities of these species. However, the expected wavelength range of Si II\*  $\lambda 1533$  falls in the blending free region. We do not detect any clear absorption line. For the main component we get  $\log N(\text{Si II}^*) \leq 12.30$  ( $3\sigma$ ).

Multi-component Voigt profile fit is performed using Si II  $\lambda \lambda 1808, 1526$ , S II  $\lambda 1253$ , Fe II  $\lambda \lambda \lambda 1608, 2249, 2260$ , Cr II  $\lambda 2066$ , Ni II  $\lambda \lambda \lambda 1741, 1709, 1751$  and Zn II  $\lambda 2026$  transitions and is shown in Fig. A4. Both the C II  $\lambda 1334, 1036$  transitions are heavily saturated and hence were not included while fitting.

The column density of Zn II  $\lambda 2026$  has negligible contribution from Cr II  $\lambda 2026$  and Mg I  $\lambda 2026$  lines. The metallicity for this DLA is  $[\text{Zn}/\text{H}] = -0.97 \pm 0.13$ . Within measurement uncertainties, this is consistent with  $[\text{Si}/\text{H}] = -0.95 \pm 0.15$  and  $[\text{S}/\text{H}] = -1.16 \pm 0.13$ . Therefore, for this systems also we do not find any indication of enhanced  $\alpha$ -element abundance compared to the Fe co-production elements. We tested the effect of possible hidden saturation as explained in Sect. 3.2. Similar to the  $z_{\text{abs}} = 2.9791$ , we find that the column densities of Zn II, Cr II, Fe II and Ni II are not dependent on the assumed  $b$ -values. However, for Si II, the presence of possible hidden saturation could increase the observed column density by upto 1 dex if  $b \leq 4 \text{ km s}^{-1}$ . While high-resolution is required to accurately measure  $N(\text{Si II})$ , a one dex higher value would lead to a  $[\text{Si}/\text{Zn}]$  ratio much above the Solar value, which is unlikely.

The dust content in this DLA can be determined from the depletion factors of iron, nickel, chromium, silicon compared to zinc. We measure,  $[\text{Cr}/\text{Zn}] = -0.40 \pm 0.18$ ,  $[\text{Ni}/\text{Zn}] = -0.73 \pm 0.24$  and  $[\text{Fe}/\text{Zn}] = -0.53 \pm 0.20$ . The moderate depletion noted here is consistent with what is seen in the halo gas in our galaxy. We also measure the dust to gas ratio  $\kappa = 10^{[\text{Zn}/\text{H}]} (1. - 10^{[\text{Fe}/\text{Zn}]}) = 10^{-1.12}$  and iron column density in dust of  $\log N_{\text{Fe}}^{\text{Dust}} = 15.48$ . Systems having metallicity,  $\kappa$  and  $N_{\text{Fe}}^{\text{Dust}}$  as measured in the present case are known to have a high probability for H<sub>2</sub> detections (see [Petitjean et al. 2006](#); [Noterdaeme et al. 2008](#)). However we do not detect H<sub>2</sub> in any of the low-ion component and we place the limiting column densities of  $\log N(\text{H}_2, J=0) \leq 15.0$  ( $5\sigma$ ) and  $\log N(\text{H}_2, J=1) \leq 15.2$  ( $5\sigma$ ) for the strongest low-ion component. We detect Ly $\alpha$  emission associated to this DLA. However, no other emission line is clearly detected. We discuss this in detail in section 5.

## 4 PROPERTIES OF THE GALAXY ASSOCIATED TO THE $z_{\text{abs}} = 2.9791$ DLA

We detect [O III]  $\lambda \lambda 4960, 5008$  emission in the spectrum obtained with the slit aligned at a position angle (PA) =  $0^\circ$  for the DLA at  $z_{\text{abs}} = 2.97919$  (See Fig. 3). The emission is seen at a projected separation of  $\sim 1.5 \pm 0.1 \text{ arc sec}$  from the QSO trace that corresponds to an impact parameter of  $\rho = 11.9 \pm 0.8 \text{ kpc}$ . The fact that the emission is not seen in spectra taken with slit oriented in other two position angles is consistent with the extent of the emitting region being smaller than 13 kpc in the East-West direction. The emission is unresolved in the spatial axis suggesting that the galaxy is compact with a size of  $\leq 4.5 \text{ kpc}$ . We do not detect other emission lines like Ly $\alpha$ , H $\beta$  and [O II]  $\lambda 3727$  at the spatial location where the [O III] emission is detected. We derive

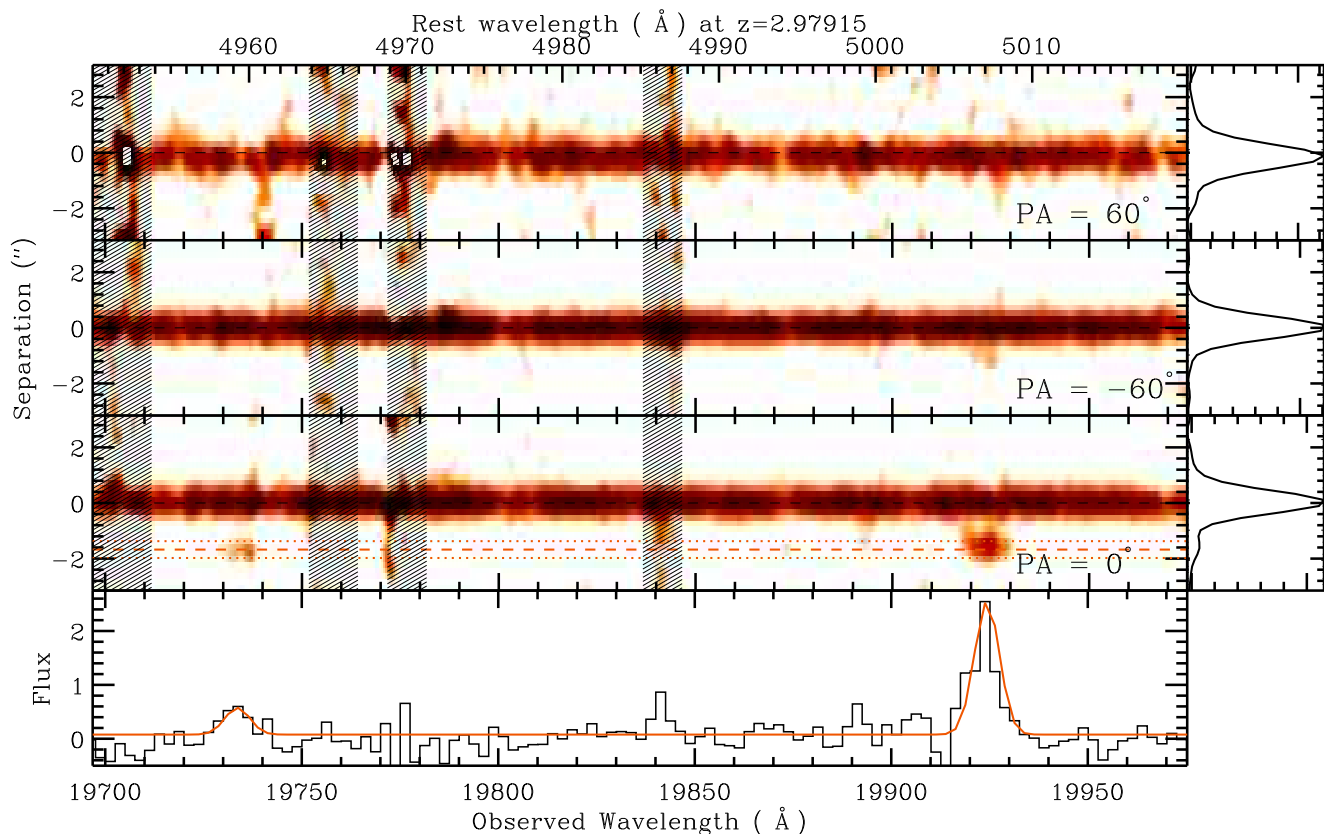


**Figure 3.** *Top three panels:* 2D spectrum of the J2358+0149 obtained with the slit oriented in three position angles (mentioned in each panel) in the expected wavelength range of [O III] emission at the redshift of the  $z_{\text{abs}} = 2.9791$  DLA. The [O III] emission, well detached from the QSO trace, is seen only for  $\text{PA} = 0^\circ$ . The trace of the galaxy is shown with a long-dashed line and the dotted lines give the  $1\sigma$  of the trace. Shaded regions mask the wavelength range affected by sky-subtraction residuals. [O III] emission lines are not detected in the spectra taken with other two position angles. *Bottom panel:* 1D spectrum extracted at the galaxy trace is shown together with a single Gaussian fit to the [O III] lines. The flux is given in units of  $10^{17} \text{ erg s}^{-1} \text{ cm}^{-2} \text{ \AA}^{-1}$ .

**Table 4.** Emission lines from the DLA galaxy at  $z_{\text{gal}} = 2.9784$

Line	Flux ( $10^{-17} \text{ erg cm}^{-2} \text{ s}^{-1}$ )	Luminosity ( $10^{42} \text{ erg s}^{-1}$ )
Ly $\alpha$	$\leq 0.64^a$	$\leq 0.58$
[O II] $\lambda 3727$	$\leq 0.19^b$	$\leq 0.15$
[H $\beta$ ] $\lambda 4862$	$\leq 0.22^b$	$\leq 0.17$
[O III] $\lambda 4960$	$0.52 \pm 0.06$	$0.41 \pm 0.04$
[O III] $\lambda 5008$	$2.02 \pm 0.15$	$1.59 \pm 0.12$

<sup>a</sup> Obtained assuming Ly $\alpha$  line spread as expected in the static medium (see text for details). <sup>b</sup> Using the line width identical to that of O III.

the [O III] line flux by fitting Gaussians to the observed line profiles (see bottom panel of Fig. 3).

In the case of other non-detected emission lines, we derive the  $3\sigma$  upper limits by assuming the line width to be similar to that of the [O III] line. As the Ly $\alpha$  emission can be much wider than the rest of the lines, due to radiative transport effects, we follow a different procedure to get its limiting flux. As can be seen in Fig. 4, no significant flux is detected along the expected trace of the emission line galaxy. If we assume the gas to be a static slab,

then the Ly $\alpha$  profile will have double humps separated by  $\sim 1200$  (respectively  $526$ )  $\text{km s}^{-1}$  if we assume the gas temperature to be  $10^4$  K (respectively for  $100$  K) for the measured  $N(\text{H I})$  (using eq. 21 of [Dijkstra 2014](#)). We integrated the flux within  $\pm 600 \text{ km s}^{-1}$  to the redshift of the [O III] emission along the spectral axis and  $\pm 2.5$  pixels in the spatial axis centered around the expected location of the trace from the [O III] emission. This gives the  $3\sigma$  flux limit of  $6.4 \times 10^{-18} \text{ erg cm}^{-2} \text{ s}^{-1}$ .

Table 4 lists the derived fluxes and corresponding luminosities of these lines. The values given are obtained without applying any dust correction or correction for slit losses. Both these will make the intrinsic luminosity of the [O III] line higher than what we infer. Till now [O III] emission is detected in 7 high- $z$  (i.e.  $z_{\text{abs}} \geq 1.9$ ) DLAs (see Table 6 of [Fynbo et al. 2013](#)). The observed [O III] luminosity in the present case is close to the median value observed among other DLAs. The main difference is that the present system has the highest  $z_{\text{abs}}$  and lowest metallicity among the high- $z$  DLAs with the detection of [O III] emission. The total [O III] luminosity is  $0.3 L_*$  as per the fit to the H $\beta$  + [O III] luminosity function given by [Khostovan et al. \(2015\)](#) for  $z \sim 3$  galaxies.

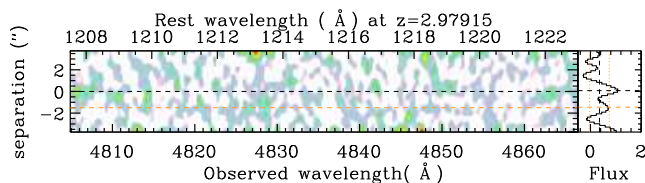


**Figure 4.** 2D-spectrum at the expected wavelength range of Ly $\alpha$  emission from the  $z_{\text{abs}} = 2.9791$  DLA obtained using the slit aligned at a PA of  $0^\circ$ . The original image is smoothed by a Gaussian filter having an FWHM of 3 pixels (i.e.  $0.6 \text{ \AA}$ ) along the wavelength axis and 5 pixel (i.e.  $0.75 \text{ arc sec}$ ) along the spatial axis. In the right hand side panel, the average flux (in units of  $10^{-19} \text{ erg s}^{-1} \text{ cm}^{-2} \text{ \AA}^{-1}$ ) is shown for each row. Based on the [O III] emission detected we expect the Ly $\alpha$  emission at the spatial separation of  $1.5 \text{ arcsec}$  from the QSO trace (shown at 0 along the y-axis).

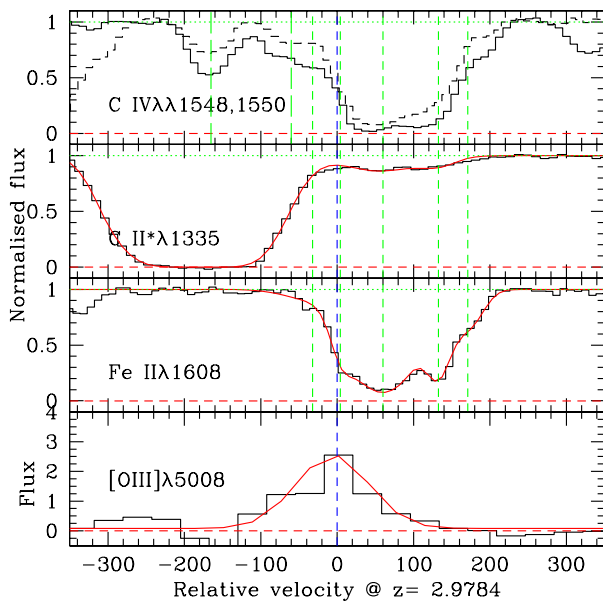


**Figure 5.** Comparison of absorption lines and [O III]  $\lambda 5008$  emission associated with the  $z_{\text{abs}} = 2.9791$  DLA. The zero velocity is defined with respect to the  $z_{\text{gal}} = 2.9784$  derived from the [O III] emission. The bottom panel shows the [O III] emission (with flux shown in the units of  $10^{-17} \text{ ergs cm}^{-2} \text{ s}^{-1} \text{ \AA}^{-1}$ ) together with the best fitted Gaussian. In the top panel, we plot profiles of both the members of the C IV doublet. Middle two panels show profiles of Fe II (as a representative of the low ionization species) and C II\* together with the best fitted Voigt profiles (as also in Fig. A2). The vertical short-dashed lines show the individual components identified for the low ions. Vertical long-dashed lines mark additional components seen only in C IV absorption.

#### 4.1 Emitting and absorbing gas kinematics

The single component Gaussian fit to the [O III] lines gives a deconvolved FWHM of  $110 \text{ km s}^{-1}$  and a velocity dispersion of  $\sigma \sim 46 \text{ km s}^{-1}$ . We can use this to estimate the dynamical mass of the galaxy within the [O III] line emitting region. For a given optical size ( $r_{\text{eff}}$ ) of the galaxy one can estimate the dynamical mass ( $M_{\text{dyn}}$ ) using the relation  $M_{\text{dyn}} \sim [3\sigma^2 r_{\text{eff}}/G]$  (see Maseda et al. 2014). As we do not have the photometric measurement of  $r_{\text{eff}}$ , we use two values for estimating the range in the dynamical mass. First, we consider  $r_{\text{eff}} \leq 4.5 \text{ kpc}$  as inferred based on the fact that the emission is unresolved in the spatial direction along

the slit. This gives  $M_{\text{dyn}} \leq 6.4 \times 10^9 M_\odot$ . At  $z \sim 3$ , typical size of LBGs are smaller than  $4.5 \text{ kpc}$  limit we have found. If we assume the typical  $r_{\text{eff}} = 1 \text{ kpc}$  (as found by Shibuya et al. 2015, for example) measured for the LBGs at these redshifts we get  $M_{\text{dyn}} \sim 1.4 \times 10^9 M_\odot$ . The inferred dynamical mass is similar to what has been seen in the extreme emission line galaxies at high- $z$  by Maseda et al. (2013).

Assuming a simple dark matter density profile  $\rho(r) \propto r^{-2}$  (isothermal profile) and normalizing the density at the optical radius to the mean density within the optical radius ( $r_{\text{eff}} = 1$  or  $4.5 \text{ kpc}$  as considered above), we find the total mass within  $12 \text{ kpc}$  to be  $3 - 4 \times 10^{10} M_\odot$ . This will mean a circular velocity of  $105 - 121 \text{ km s}^{-1}$  at  $12 \text{ kpc}$ . In Fig. 5 we compare the emission line profile from the galaxy to the absorption profile measured along the QSO sight line. It is clear that almost all the low-ion absorption are redshifted with respect to the systemic redshift of the galaxy defined by the centroid of the [O III] emission lines (i.e.  $z_{\text{em}} = 2.9784$ ). Specifically, individual Voigt profile components used to fit the low ion absorption have redshifted velocities of  $-32, 4.2, 60, 132.6$  and  $171.1 \text{ km s}^{-1}$ . In addition to these components C IV absorption has components at  $-60$  and  $-160 \text{ km s}^{-1}$ . Considerable absorption of low and high ions originate outside the circular velocity we inferred above. Therefore, it is most unlikely that the absorption originates from an extended co-rotating disk.

It is possible that the absorbing gas may originate either from the large scale infall or outflow as usually suggested for the “ultra-strong” Mg II absorbers (Gauthier & Chen 2012; Bouché et al. 2012; Kacprzak et al. 2012; Bouché et al. 2013). In these cases, galaxy rotational velocity, orientation of the galaxy with respect to the QSO sight line are used in addition to the absorption kinematics to draw conclusions on the nature of the gas flow. In the absence of the galaxy image it will be difficult to draw firm conclusions on the nature of the gas flow in the present case.

In addition, the spatially unresolved [O III] emission we detect may originate from a star forming clump that may be from a region away from the centre of a massive quiescent galaxy like the one found by Zanella et al. (2015). Therefore, it is of utmost importance to have deep imaging to get further insights into the nature of this galaxy.

#### 4.2 Star formation rate

As we detect only [O III] lines we use the upper limits on [O II] and H $\beta$  to infer the upper limit on the star formation rate. We will use standard relationships used in the literature assuming Salpeter IMF in this study. The calibration between [O III] luminosity and SFR (derived from other tracers) is recently established in the case of high- $z$  LBGs (see for example, Suzuki et al. 2015) and GRB host galaxies (Krühler et al. 2015). If we use these relationships we get  $6.6 \leq \text{SFR} (M_\odot \text{ yr}^{-1}) \leq 25$ . From the  $3\sigma$  limit on the [O II] luminosity we derive a star formation rate (SFR) of  $\leq 2.1 M_\odot \text{ yr}^{-1}$  using the relationship given by Kennicutt (1998). Similarly if we use the standard Balmer ratio of 2.8 and the relationship between H $\alpha$  luminosity and SFR given by Kennicutt (1998) we derive  $\text{SFR} \leq 3.8 M_\odot \text{ yr}^{-1}$  for the  $3\sigma$  upper limit on the H $\beta$  luminosity. The wide range in SFR derived above reflects the fact that ionized gas in the present case is highly excited compared to what is typically seen. We discuss this in detail in the next section.

We can also estimate the upper limit on SFR in the DLA galaxy using the inferred upper limit on the Ly $\alpha$  line flux assuming that the Ly $\alpha$  photons mainly originate from the H II regions around massive stars and case B recombination (Osterbrock & Ferland



2006). The Ly $\alpha$  luminosity ( $L_{Ly\alpha}$ ) is then related to the SFR ( $\dot{M}_{SF}$ ) by,

$$L(Ly\alpha) = 0.68 h\nu_{\alpha} (1 - f_{esc}) N_{\gamma} \dot{M}_{SF} \quad (1)$$

where  $h\nu_{\alpha} = 10.2$  eV,  $f_{esc}$  and  $N_{\gamma}$  are, respectively, the energy of a Ly $\alpha$  photon, the escape fraction of Lyman continuum photons and the number of ionizing photons released per baryon of star formation. We use  $f_{esc} = 0.1$  and  $N_{\gamma} = 7880$  that is appropriate for the measured metallicity of the DLA (from Table 1 of Samui et al. 2007). Thus the observed Ly $\alpha$  luminosity gives an upper limit on the star formation rate,  $\dot{M}_{SF} \leq 4 (f_{esc}^{Ly\alpha}/0.05) M_{\odot} yr^{-1}$ .

The non-detection of stellar continuum in the visible part of the spectrum places a constraint on the flux at the rest frame 1500 Å of the galaxy. However the implied limit on the star formation rate is not stringent (i.e.  $\leq 27 M_{\odot} yr^{-1}$ ). All this suggests that the DLA galaxy is forming stars at moderate rate. The strong [O III] emission seen in this system may be related to the high excitation in the ionized gas. We discuss this in detail in the following section.

### 4.3 High [O III]/[O II] ratio and metallicity

The most interesting aspect of the present system is the very large value (i.e.  $\geq 10$ ) of the [O III]/[O II] and [O III]/[H $\beta$ ] ratios. It is well documented now that  $z > 2$  galaxies tend to have elevated [O III]/[O II] ratio compared to local star forming galaxies (see for example, Steidel et al. 2014; Masters et al. 2014). However, galaxies with this ratio greater than 10 are rare.

In the local universe, such high ratios (in the range 10-50) are seen in ‘extreme blue compact dwarf galaxies (BCDs)’. It has also been pointed out that these extreme BCDs are compact, have low metallicity and high specific star formation as found in high- $z$  LBGs. High excitations seen in low- $z$  BCDs and high- $z$  galaxies may be attributed to many possibilities such as low metallicity, high ionization parameter, hard ionizing radiation field and/or the presence of a density-bound H II regions (Stasińska et al. 2015).

Narrow velocity width of the [O III] line probably rules out the possibility of excitation due to a hidden AGN. Also the absence of [O II] line rules out the strong [O III]/[H $\beta$ ] being due to elevated oxygen abundance. Recently it was suggested that systems with elevated [O III]/[O II] ratio may have large Lyman continuum (LyC) escape fraction if the gas is optically thin (i.e. matter bound H II regions). Such galaxies will also show strong Ly $\alpha$  emission as its escape fraction is also enhanced due to optical depth being low (see for example, Jaskot & Oey 2014; de Barros et al. 2016). Indeed, in the  $z_{em} = 3.2$  Lyman continuum leaking galaxy studied by de Barros et al. (2016) the observed  $L[O III]/L[O II]$  and  $L[O III]/L[H\beta]$  ratios are consistent with our galaxy. However, Ly $\alpha$  emission is clearly detected with  $L[O III]/L(Ly\alpha) = 1.4$ . Our observations rule out such a ratio by more than  $7\sigma$  level. Therefore, it is most unlikely that the elevated [O III] luminosities seen in the present case may be due to matter bound line emitting nebula.

Stanway et al. (2014) have argued that the high [O III]/H $\beta$  ratio can be explained through the ageing of a rapidly formed stellar population. The probability of detection of galaxies with high [O III]/H $\beta$  depends on the time-scale over which such elevated ratios are maintained in the star bursting region. They showed that the inclusion of binary evolution in the stellar synthesis code enhances this duration up to few 100 Myrs. It is interesting that even in their model one needs high densities and low metallicity in the ISM to get such large [O III]/H $\beta$  ratios. In this scenario the present system could have gone through a recent star burst activity

with a relatively metal poor ageing stellar population surrounded by a dense interstellar medium.

Using the IZI (Inferring the gas phase metallicity (Z) and ionization parameter of the ionized nebula) code described in Blanc et al. (2015) and assuming the photoionization model results of Levesque et al. (2010) we derive constraints on the nebular metallicity (i.e.  $12 + [O/H] \leq 8.5$ ), ionization parameter (i.e.  $\log q > 8.14$  and  $\log U \geq -2.33$ ). Such large ionization parameters are inferred in  $\leq 25\%$  of the  $z \geq 2$  galaxies studied by Masters et al. (2014). The upper limit on metallicity is consistent with the metallicity we derive for the DLA along the QSO line of sight. While we need to detect other nebular lines with deep spectroscopic observations to draw firm conclusions on the physical conditions in this DLA galaxy, all indications are suggesting the galaxy to be compact, moderately star forming and having low metallicity and high specific star formation rate.

### 4.4 C II\* cooling rate:

Associated C II\*  $\lambda 1335$  absorption is clearly detected in this DLA (see Fig. 5). Using Voigt profile fits we obtain  $\log N(C II^*) = 13.64 \pm 0.07$ . This together with the total  $N(H I)$  measured gives a cooling rate  $\log l_c = -27.57 \pm 0.12$  ergs  $s^{-1} H^{-1}$ . Wolfe et al. (2008) have proposed a bimodal distribution in DLA population based on [C II] cooling rate  $l_c$ : “low-cool” DLAs with  $l_c \leq l_c^{crit}$  and “high-cool” DLAs with  $l_c > l_c^{crit}$  (where  $l_c^{crit} = 10^{-27}$  ergs  $s^{-1} H^{-1}$ ). The cooling rate inferred for the present DLA belongs to the “low-cool” population. The metallicity and cooling rate inferred in the present case is close to that of the  $z_{abs} = 2.5397$  system toward J1004+0018 studied by Dutta et al. (2014). We can use the model results presented in their Fig. 14 to interpret C II\* observations for the present system. The observed ratio,  $\log N(C II^*)/N(Si II) = -1.85 \pm 0.25$  and the cooling rate can be explained with a radiation field similar to Galactic mean UV field and a hydrogen density of  $1 \text{ cm}^{-3}$ . Therefore, the absorbing gas (if part of a cold neutral medium) is seeing excess radiation either from the galaxy or from the ongoing in situ star formation.

Following Wolfe et al. (2008) we can write,

$$l_c = 10^{-5} \kappa \epsilon J_V, \quad (2)$$

where,  $\kappa = 0.018$ ,  $\epsilon$  and  $J_V$  are dust to gas ratio, grain heating efficiency and local background radiation field intensity respectively. When we use the maximum dust efficiency (i.e. 2%) in the cold neutral medium found by Weingartner & Draine (2001) we get  $J_V^{local} = 3.1 \times 10^{-20}$  erg  $s^{-2} \text{ cm}^{-2} \text{ Hz}^{-1}$ . If we further use equation 3 of Wolfe et al. (2008) we get the in-situ surface star formation rate,  $\Sigma_{SFR} = 2 \times 10^{-4} M_{\odot} \text{ yr}^{-1} \text{ kpc}^{-2}$ . Although very small, our present observations can not rule out such a low SFR along the QSO sightline. Alternatively if the gas is not part of the stellar disk (as it is most likely) then the photo-heating can come from the galaxy light and in particular the [O III] emitting region. Such a scenario has been proposed to explain the physical conditions in low- $z$  quasar-galaxy pairs (see for example, Dutta et al. 2015).

However, if absorbing gas detected along the QSO sight line is part of an infalling or outflowing gas, then C II\* may be originating from a warm or partially ionized gas as suggested by Srianand et al. (2005) in the case of H $_2$  bearing DLAs. If that is the case then we will not have much handle on the star formation rate from the C II\* cooling rate. This again suggests that purely based on the C II\* detection alone we will not be able to conclude that the absorbing gas is part of the cold ISM.

## 5 Ly $\alpha$ EMISSION FROM THE DLA AT $z_{\text{abs}} = 3.2477$

In the combined 1D spectrum we see some residual flux at the bottom of the Ly $\alpha$  line of  $z_{\text{abs}} = 3.2477$  DLA (see bottom panel in Fig. 6). In the top panel of Fig 6 we plot the 2D-Gaussian smoothed (with a FWHM of 5 pixels along the spatial direction and 3 pixels along the observed wavelength) combined 2D spectrum obtained with slits aligned at three different position angles. The overlaid contours are at the flux levels 2, 4, 6, 8, 10, 12,  $14 \times 10^{-20}$  erg s $^{-1}$  cm $^{-2}$  Å $^{-1}$ . Excess flux is clearly seen in the wavelength range where we found residuals in the 1D spectrum. It is also clear from the images that most of the residual flux found is close to the trace suggesting that the Ly $\alpha$  emitting source is very close to our line of sight to the QSO. In order to estimate the significance of the Ly $\alpha$  emission we considered 9 apertures as shown by boxes in Fig. 6. Each aperture is 6 Å wide in the observed wavelength and 1.75 arc sec in the spatial direction. As expected the integrated flux ( $4.5 \times 10^{18}$  erg s $^{-1}$  cm $^{-2}$ ) is maximum for the middle aperture and is 6 times higher than the average flux [i.e.  $(0.72 \pm 0.17) \times 10^{-18}$  erg s $^{-1}$  cm $^{-2}$ ] of the remaining 8 apertures. As can be seen from the figure the peak emission is  $\sim 0.4$  arc sec away from the center of the QSO trace.

In order to understand the possible spatial separation between the Ly $\alpha$  emission and the QSO we repeated the above exercise on the 2D spectra obtained at different slit orientations. In the case of spectra obtained with position angles (PA)  $0^\circ$  and  $-60^\circ$  we detect maximum flux in the middle aperture with the mean flux of the other 8 apertures less by about a factor of 3. We do not detect significant excess emission in the middle aperture in the case of PA =  $60^\circ$ . But the flux errors are large and flux measured in other two position angles are consistent within  $1.5\sigma$  for the non-detection. In the case of PA =  $0^\circ$  the peak emission is at 0.5 arc sec below the QSO trace. In the case of PA =  $-60^\circ$  the emission is concentrated in two blobs one above and one below the trace (with the off-set of  $\leq 0.6$  arc sec). This suggests that the Ly $\alpha$  emission is extended and off-centred with respect to the QSO position. While we need a better S/N spectrum to perform triangulation the present data suggests that the emitting region is within  $\sim 5$  kpc of the QSO line of sight.

It is well known that, due to complex radiative transport, the profile of the Ly $\alpha$  emission will not be a simple Gaussian. However, for simplicity we fit the Ly $\alpha$  line in the 1D spectrum with a single Gaussian. The fit is also shown in the bottom panel of Fig. 6. The centroid of the Gaussian gives  $z_{\text{em}} = 3.2512 \pm 0.0004$  and the integrated Ly $\alpha$  flux is  $(5.04 \pm 0.90) \times 10^{-18}$  ergs cm $^{-2}$  s $^{-1}$ . This confirms the emission at the  $5\sigma$  level. This corresponds to a luminosity of  $(4.5 \pm 0.8) \times 10^{41}$  erg s $^{-1}$ . Instead of fitting the Gaussian, if we simply measure the total flux in the bottom of the Ly $\alpha$  absorption trough, we find the total flux to be  $(7.2 \pm 1.3) \times 10^{-18}$  ergs cm $^{-2}$  s $^{-1}$  and the corresponding luminosity is  $(6.4 \pm 1.2) \times 10^{41}$  erg s $^{-1}$ . Finley et al. (2013) have found a strong Ly $\alpha$  emission in 25% of the pDLAs with  $\log N(\text{H I}) \geq 21.3$ . Their analysis favor these DLAs being associated with the host galaxies of the QSOs and probably not completely covering the Ly $\alpha$  from the narrow line regions (NLR). The Ly $\alpha$  flux measured in the present case is nearly 35 times less than the average flux measured by Finley et al. (2013) and probably do not belong to the pDLA population identified by them.

The Ly $\alpha$  emission is roughly 280 km s $^{-1}$  blue shifted with respect to the QSO based on the redshift of the QSO measured from the Mg II emission line peak. However, the Ly $\alpha$  emission is redshifted by about 320 km s $^{-1}$  with respect to the strongest

absorption component. For the observed value of  $N(\text{H I})$  for this system, if we assume the DLA to be a static medium having a kinetic temperature of  $10^4$  K then we expect the Ly $\alpha$  emission to have a double hump with the peak in the red wing shifted by about 375 km s $^{-1}$  (see Dijkstra 2014). This is roughly consistent with the shift we notice above between the redshift of the Ly $\alpha$  emission and metal absorption lines. It is also interesting to note that the peak Ly $\alpha$  emission occurs just outside the maximum velocity of the low ions (see Fig. 7) consistent with what one would have expected based on the Ly $\alpha$  line transport.

In a simple radiative transport model, this can be understood in terms of scattering from an expanding (i.e. outflowing) H I shell. However the actual radiative transport may be a bit more complex when the medium is not static and has dust. In addition, the Ly $\alpha$  emission could come either from the star forming regions in the DLA or from the fluorescence induced by the QSO UV flux if the absorber is very close to the QSO. We discuss both the possibilities.

### 5.1 Star formation rate

First we consider the possibility that the observed Ly $\alpha$  emission originates from an intervening galaxy. In that case, we estimate the average SFR in the DLA,  $M_{\text{SF}} \sim 0.17 - 0.23 M_{\odot} \text{yr}^{-1}$ , using the prescription described in Section 4.2. The range comes from the luminosities estimated using the simple integration and the single component Gaussian fit to the Ly $\alpha$  emission. Only a small fraction of Ly $\alpha$  generated in the galaxy escapes the galaxy and some fraction of this emerging Ly $\alpha$  photons are also absorbed by the IGM. Therefore, the above derived star formation rate without making any corrections for the radiative transport should be considered as a lower limit.

We detect neither [O II] nor [O III] emission. As the expected position of H $\beta$  coincides with the H $\beta$  emission from the QSO it is difficult to estimate the H $\beta$  luminosity associated to the DLA. From the rms in the expected position of the [O II] line in the QSO continuum we obtain a  $3\sigma$  upper limit on the [O II] luminosity of  $1.2 \times 10^{41}$  ( $3\sigma$ ) erg s $^{-1}$ . If we use the relationship given by Kennicutt (1998) this translates to an upper limit in the star formation rate of  $1.7 M_{\odot} \text{yr}^{-1}$ . This implies that the Ly $\alpha$  escape fraction is more than 10% if we use the Ly $\alpha$  luminosity based on Gaussian fits or  $\geq 14\%$  if we use the integrated Ly $\alpha$  luminosity. Inclusion of corrections for dust extinction and the Ly $\alpha$  opacity of the IGM will further increase this lower limit.

The lower limit we find here is higher than the mean measured value (i.e.  $f_{\text{esc}}^{\text{Ly}\alpha} \sim 5\%$ ) in the high- $z$  LBGs (Hayes et al. 2010). However, such high values of  $f_{\text{esc}}^{\text{Ly}\alpha}$  are also seen in a couple of high- $z$  DLAs [i.e.  $f_{\text{esc}}^{\text{Ly}\alpha} = 55\%$  in the case of  $z_{\text{abs}} = 2.35$  DLA towards Q 2222-0946 (Fynbo et al. 2010) and  $f_{\text{esc}}^{\text{Ly}\alpha} = 20\%$  in the case of  $z_{\text{abs}} = 2.21$  DLA towards Q1135-0010 (Noterdaeme et al. 2012a)]. However, unlike the present case the inferred SFR based on the emission lines detected in the NIR in these cases are very high (i.e.  $\geq 10 M_{\odot} \text{yr}^{-1}$ ).

### 5.2 Fluorescent Ly $\alpha$ emission induced by the quasar

The fluorescent Ly $\alpha$  emission induced by the QSO is a viable alternative, in particular if the escape fraction of Ly $\alpha$  is very small. We explore this possibility here.

To start with, we note that the size and surface brightness of the Ly $\alpha$  emission seen are both less than what is typically seen in the case of radio-loud QSOs at similar redshifts (see for example,

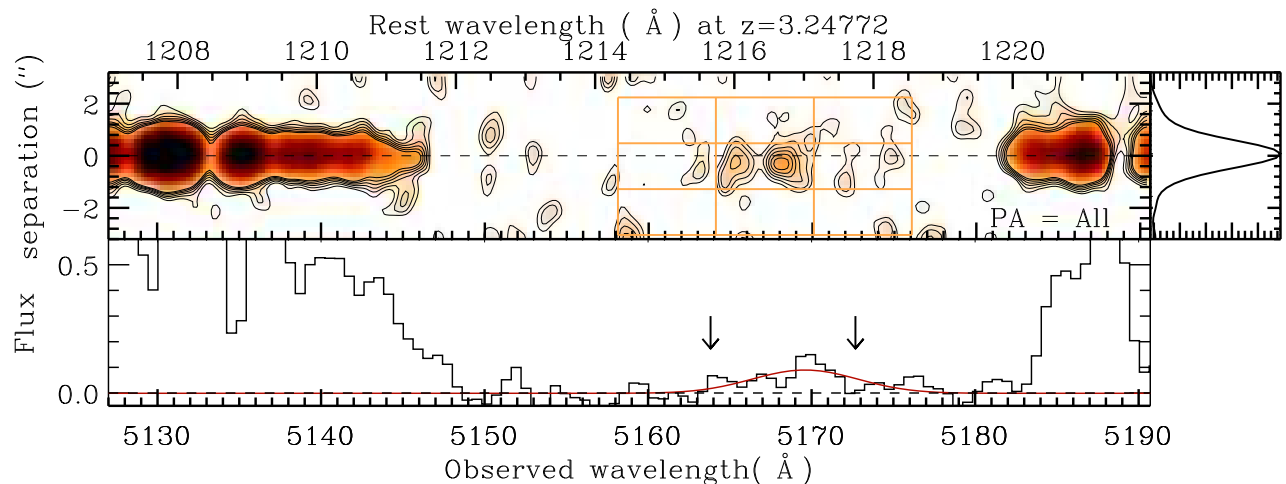


**Figure 6.** The Ly $\alpha$  emission from  $z_{\text{abs}} = 3.2477$  DLA towards J2358+0149. In the top panel we show the 2D image of the QSO in the wavelength range of the Ly $\alpha$  emission observed in the combined 2D spectra obtained with three slit orientations. We clearly see excess flux in the regions identified by the middle box. In the bottom panel, we plot the extracted 1D spectrum and a single component Gaussian fits to the residual flux in the bottom of the DLA profile. The two arrows show the locations of the metal absorption redshift and QSO emission redshift.

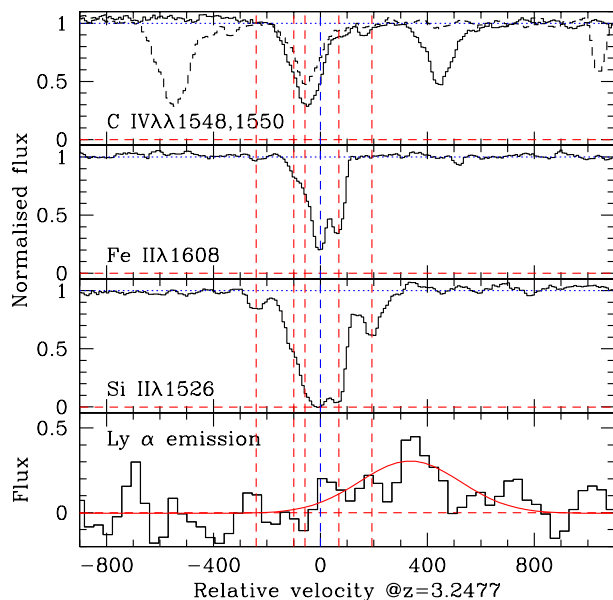


**Figure 7.** Comparison of absorption lines and the Ly $\alpha$  emission associated with the  $z_{\text{abs}} = 3.2377$  DLA. The zero velocity is defined with respect to the  $z_{\text{abs}} = 3.2477$ . The bottom panel shows the Ly $\alpha$  emission (with flux shown in the units of  $10^{-17}$  ergs  $\text{cm}^{-2}$   $\text{s}^{-1}$   $\text{\AA}^{-1}$ ) together with the best fitted Gaussian. In the top panel, we plot profiles of both the members of the C IV doublet. Middle two panels show profiles of Fe II and Si II (as a representative of the low ionization species). The vertical short-dashed lines show the individual components identified for the low ions.

Roche et al. 2014). This suggests that the origin of Ly $\alpha$  emission in the present case may be very different from the extended Ly $\alpha$  seen around radio galaxies. We also note that, based on the surface brightness of the Ly $\alpha$  emission, lack of NV absorption and fine-structure lines of Si II, this DLA is not similar to the one studied by Fathivavsari et al. (2015), where the DLA is thought

to be dense, compact and close to the QSO covering the broad as well as narrow emission line region only partially (see also, Finley et al. 2013). Therefore, it is most likely that we are not seeing the extended NLR of the host galaxy.

For the set of cosmological parameters assumed in this work, if we consider the redshift difference between the DLA and the QSO to be due to spatial separation then we expect the DLA to be 1.8 Mpc away from the QSO. As some part of the redshift difference may come from the peculiar velocities the actual separation can be slightly different.

From our flux calibrated spectrum and SDSS spectrum we infer the flux at 912  $\text{\AA}$  in the rest frame of the QSO to be  $2.3 \times 10^{-16}$  erg  $\text{cm}^{-2}$   $\text{s}^{-1}$   $\text{\AA}^{-1}$ . Assuming the UV spectrum of the QSO to be a power-law,  $J_{\nu} \propto \nu^{-1.4}$ , we estimate the H I photoionization rate as a function of distance in Mpc,  $r_{\text{Mpc}}$ , as  $\Gamma_{\text{HI}}^{\text{Q}} = 1.14 \times 10^{-11} / r_{\text{Mpc}}^2$  ( $\text{s}^{-1}$ ). From the recent computations of UV-background using updated QSO and galaxy emissivities (see Khaire & Srianand 2015b,a), we estimate the hydrogen photoionization rate due to the background to be  $\Gamma_{\text{HI}}^{\text{bgr}} = 6.9 \times 10^{-13}$  ( $\text{s}^{-1}$ ). The two rates are equal for  $r_{\text{Mpc}} = 4.06$ . Therefore, in the absence of in situ star formation, the DLA will receive at least 5 times more ionizing photons from the QSO compared to that from the background. Therefore, at face value the observed Ly $\alpha$  originating from fluorescence is a realistic possibility.

The fluorescence induced Ly $\alpha$  emission around radio-quiet QSOs have been reported in a few cases (see for example, Adelberger et al. 2006; Francis & McDonnell 2006; Cantalupo et al. 2012, 2014). Typically one looks for: (i) large Ly $\alpha$  line equivalent width mainly due to the absence of a strong continuum, (ii) profiles showing double humps and (iii) large surface brightness, to identify the candidate fluorescence Ly $\alpha$  emitters. As the Ly $\alpha$  emission is very close to the QSO trace, it is very difficult to measure the equivalent width in the present case. We do observe that the Ly $\alpha$  emission peak is shifted with respect to the metal line absorption from the DLA. However this alone will not confirm the fluorescence as such a profile is also expected

from the radiative transport even in the case of Ly $\alpha$  induced by the embedded stars.

Following Shull et al. (2014), we can write the integrated unidirectional flux of the H I ionizing photons,  $\phi_0 = \int_{\nu_0}^{\infty} \pi I_{\nu} d\nu / h\nu$ . We estimate  $\phi_0 \sim 84960$  photons for the meta-galactic UV background at  $z \sim 3.2$ . If we assume a one arcsec<sup>2</sup> optically thick slab of H I gas in photoionization equilibrium with this background then we get a surface brightness,  $SB_{\text{Bg}} \sim 1.9 \times 10^{-20} \text{ erg s}^{-1} \text{ cm}^{-2} \text{ arcsec}^{-2}$ , if the disk is seen face-on. Otherwise there will be a dilution factor that is a ratio of projected area along the line of sight to the actual area. Here,  $SB_{\text{Bg}}$  is the surface brightness expected purely due to the UV background radiation.

The observed surface brightness of the Ly $\alpha$  emission in the present case is  $2.9 \times 10^{-18} \text{ erg s}^{-1} \text{ cm}^{-2} \text{ arcsec}^{-2}$ . In general, the surface brightness induced by the QSO fluorescence can be written as  $SB = (1 + b) SB_{\text{Bg}}$ , where the factor  $b$  is just  $\Gamma_{\text{HI}}^{\text{Q}} / \Gamma_{\text{HI}}^{\text{Bg}}$ . In the present case, for the face on condition, we find  $b \sim 142$  and the cloud has to be at a distance of 340 kpc from the QSO. Therefore, the Ly $\alpha$  emission seen in the present case can be produced by the QSO fluorescence if the gas is at  $\sim 340$  kpc from the QSO. However, the exact value will depend on the assumed geometry of the absorbing gas and the projected area towards the QSO and along the line-of-sight. Spatially resolved detection of associated stellar light, better mapping of the Ly $\alpha$  emission and detection of other emission lines with deeper spectroscopic observations will allow us to test the fluorescence scenario more thoroughly.

## 6 SUMMARY AND DISCUSSIONS

Using long-slit spectroscopic observation of J2358+0149 ( $z_{\text{em}} = 3.255$ ), obtained in three different position angle with VLT-X-shooter, we have searched for emission lines originating from four DLAs and one sub-DLA in the redshift range 2.73–3.25. In this work we have presented the column density, metallicity and depletion measurements for all the 5 systems. We reported the detection of emission lines associated with two DLAs having,  $\log N(\text{H I}) > 21.0$ , with low ion absorption lines showing large velocity widths (i.e.  $\Delta v_{90} > 140 \text{ km s}^{-1}$  for the Fe II  $\lambda 1608$  line). We do not detect any emission in the remaining three systems that have low  $N(\text{H I})$  and narrow metal line widths.

In the case of  $z_{\text{abs}} = 2.9791$  ESDLA, that also satisfies the definition of “*ultra-strong*” Mg II-systems, we detect [O III]  $\lambda\lambda 4960, 5008$  emission at a projected separation of  $11.9 \pm 0.8$  kpc from the QSO sight line. The absorbing gas has a metallicity of  $[\text{Zn}/\text{H}] = -1.83 \pm 0.18$  and moderate dust depletion (i.e.  $[\text{Zn}/\text{Fe}] = 0.15 \pm 0.25$ ). The absence of [O II] and H $\beta$  emission suggests that the galaxy is a high-excitation galaxy, similar to the “*extreme blue compact dwarf*” galaxies seen at the low- $z$ , undergoing a moderate star formation ( $\text{SFR} \leq 2.1 M_{\odot} \text{ yr}^{-1}$ ). The large, [O III]/[O II]  $\geq 10$  and [O III]/H $\beta$   $\geq 10$  ratios seen, are very rare even among high- $z$  LBGs that usually show elevated ratios compared to their low- $z$  counterparts. Based on the absence of He II, C IV, Ly $\alpha$  and Mg II emission we feel the hidden AGN contribution to the excitation is least likely. We also do not favor the matter bound ionized region scenario as one would expect a strong Ly $\alpha$  emission in this case. Considerable progress can be made if one can detect other emission lines and image the galaxy in the continuum light using deep observations. This will allow us to measure the metallicity and ionization parameter of the nebula and constrain the nature of the star formation in this galaxy. In addition, one will be able to understand the origin of the large velocity spread seen in the

absorption lines in terms of cold accretion or large scale outflows. This will allow us to build a consistent model of this system.

In the case of  $z_{\text{abs}} = 3.2477$  proximate DLA we detect extended and diffuse Ly $\alpha$  emission in the DLA trough. The DLA has a metallicity of  $[\text{Zn}/\text{H}] = -0.97 \pm 0.13$  and moderate depletion  $[\text{Zn}/\text{Fe}] = 0.53 \pm 0.20$ . As in the previous case the metal line absorption has a very large spread and observed Mg II equivalent widths are consistent with the system being called an “*ultra-strong*” Mg II-system. The peak of the Ly $\alpha$  emission is redshifted by about  $330 \text{ km s}^{-1}$  with respect to the strongest low-ion absorption component. This is consistent with what is expected from the simple radiative transport models with gas outflow. As the absorber is very close to the systemic redshift of the QSO we have two viable scenarios for the origin of Ly $\alpha$  emission: from in situ star formation in the DLA galaxy or Ly $\alpha$  fluorescence induced by the QSO. In the former case we use the Ly $\alpha$  luminosity to estimate the star formation rate in the range  $0.17\text{--}0.23 M_{\odot} \text{ yr}^{-1}$  assuming  $f_{\text{esc}}^{\text{Ly}\alpha} = 1$ . Based on the lack of [O II] emission line we derive  $\text{SFR} \leq 1.7 M_{\odot} \text{ yr}^{-1}$  and  $f_{\text{esc}}^{\text{Ly}\alpha} \geq 0.29$ . The latter is higher than what is typically measured in high- $z$  LBGs (Hayes et al. 2010) but consistent with what is seen in the case of  $z_{\text{abs}} = 2.207$  DLA towards SDSS J113520.39-001053.56 (Noterdaeme et al. 2012a). We show that the Ly $\alpha$  fluorescence, caused by the QSO, can also reproduce the observed Ly $\alpha$  emission, provided the absorbing gas lies no more than 340 kpc from the QSO. While the exact physical situation in the present case may not be similar to what is seen in the radio-loud QSOs or in the compact proximate DLAs that do not cover the narrow line emission regions, present data does not rule out the fluorescence scenario. Detecting or placing a deep limit on the continuum emission is important to choose between the two viable alternatives discussed here. High resolution spectra of the QSO is also needed to get accurate metallicity and gas kinematics based on the absorption lines.

## 7 ACKNOWLEDGMENT

TH wishes to thank IUCAA for hospitality. We thank Sussana Vergani for her help in preparing the observational blocks. We thank the anonymous referee for useful comments.

## References

- Adelberger K. L., Steidel C. C., Kollmeier J. A., Reddy N. A., 2006, *ApJ*, **637**, 74
- Arabsalmani M., Møller P., Fynbo J. P. U., Christensen L., Freudling W., Savaglio S., Zafar T., 2015, *MNRAS*, **446**, 990
- Asplund M., Grevesse N., Sauval A. J., Scott P., 2009, *ARA&A*, **47**, 481
- Blanc G. A., Kewley L., Vogt F. P. A., Dopita M. A., 2015, *ApJ*, **798**, 99
- Bouché N., Hohensee W., Vargas R., Kacprzak G. G., Martin C. L., Cooke J., Churchill C. W., 2012, *MNRAS*, **426**, 801
- Bouché N., Murphy M. T., Kacprzak G. G., Péroux C., Contini T., Martin C. L., Dessauges-Zavadsky M., 2013, *Science*, **341**, 50
- Bunker A. J., Warren S. J., Clements D. L., Williger G. M., Hewett P. C., 1999, *MNRAS*, **309**, 875
- Cantalupo S., Lilly S. J., Haehnelt M. G., 2012, *MNRAS*, **425**, 1992
- Cantalupo S., Arrigoni-Battaia F., Prochaska J. X., Hennawi J. F., Madua P., 2014, *Nature*, **506**, 63
- Christensen L., Noterdaeme P., Petitjean P., Ledoux C., Fynbo J. P. U., 2009, *A&A*, **505**, 1007
- Christensen L., Møller P., Fynbo J. P. U., Zafar T., 2014, *MNRAS*, **445**, 225
- Cooke R., Pettini M., Steidel C. C., Rudie G. C., Nissen P. E., 2011, *MNRAS*, **417**, 1534

- Crighton N. H. M., et al., 2015, *MNRAS*, **452**, 217
- Dekel A., et al., 2009, *Nature*, **457**, 451
- Dijkstra M., 2014, *PASA*, **31**, 40
- Dutta R., Srianand R., Rahmani H., Petitjean P., Noterdaeme P., Ledoux C., 2014, *MNRAS*, **440**, 307
- Dutta R., Srianand R., Muzahid S., Gupta N., Momjian E., Charlton J., 2015, *MNRAS*, **448**, 3718
- Ellison S. L., Prochaska J. X., Hennawi J., Lopez S., Usher C., Wolfe A. M., Russell D. M., Benn C. R., 2010, *MNRAS*, **406**, 1435
- Erb D. K., Steidel C. C., Shapley A. E., Pettini M., Reddy N. A., Adelberger K. L., 2006, *ApJ*, **646**, 107
- Fathivavsari H., Petitjean P., Noterdaeme P., Pâris I., Finley H., López S., Srianand R., Sánchez P., 2015, *MNRAS*, **454**, 876
- Finley H., et al., 2013, *A&A*, **558**, A111
- Fox A. J., Ledoux C., Petitjean P., Srianand R., 2007, *A&A*, **473**, 791
- Francis P. J., McDonnell S., 2006, *MNRAS*, **370**, 1372
- Fumagalli M., O'Meara J. M., Prochaska J. X., Rafelski M., Kanekar N., 2015, *MNRAS*, **446**, 3178
- Fynbo J. P. U., et al., 2010, *MNRAS*, **408**, 2128
- Fynbo J. P. U., et al., 2013, *MNRAS*, **436**, 361
- Gauthier J.-R., 2013, *MNRAS*, **432**, 1444
- Gauthier J.-R., Chen H.-W., 2012, *MNRAS*, **424**, 1952
- Goldoni P., Royer F., François P., Horrobin M., Blanc G., Vernet J., Modigliani A., Larsen J., 2006, in *SPIE Conf. Ser.*, doi:10.1117/12.669986
- Guimarães R., Petitjean P., de Carvalho R. R., Djorgovski S. G., Noterdaeme P., Castro S., Poppe P. C. D. R., Aghaee A., 2009, *A&A*, **508**, 133
- Hartoog O. E., Fynbo J. P. U., Kaper L., De Cia A., Bagdonaite J., 2015, *MNRAS*, **447**, 2738
- Hayes M., et al., 2010, *Nature*, **464**, 562
- Jaskot A. E., Oey M. S., 2014, *ApJ*, **791**, L19
- Kacprzak G. G., Churchill C. W., Nielsen N. M., 2012, *ApJ*, **760**, L7
- Kanekar N., et al., 2014, *MNRAS*, **438**, 2131
- Kennicutt Jr. R. C., 1998, *ARA&A*, **36**, 189
- Kereš D., Katz N., Weinberg D. H., Davé R., 2005, *MNRAS*, **363**, 2
- Khairé V., Srianand R., 2015a, *MNRAS*, **451**, L30
- Khairé V., Srianand R., 2015b, *ApJ*, **805**, 33
- Khostovan A. A., Sobral D., Mobasher B., Best P. N., Smail I., Stott J. P., Hemmati S., Nayyeri H., 2015, *MNRAS*, **452**, 3948
- Krogager J.-K., Fynbo J. P. U., Møller P., Ledoux C., Noterdaeme P., Christensen L., Milvang-Jensen B., Sparre M., 2012, *MNRAS*, **424**, L1
- Krogager J.-K., et al., 2013, *MNRAS*, **433**, 3091
- Krühler T., et al., 2015, *A&A*, **581**, A125
- Kulkarni V. P., Hill J. M., Schneider G., Weymann R. J., Storrie-Lombardi L. J., Rieke M. J., Thompson R. I., Jannuzi B. T., 2000, *ApJ*, **536**, 36
- Ledoux C., Petitjean P., Srianand R., 2003, *MNRAS*, **346**, 209
- Ledoux C., Petitjean P., Fynbo J. P. U., Møller P., Srianand R., 2006, *A&A*, **457**, 71
- Levesque E. M., Kewley L. J., Larson K. L., 2010, *AJ*, **139**, 712
- Lowenthal J. D., Hogan C. J., Green R. F., Woodgate B., Caulet A., Brown L., Bechtold J., 1995, *ApJ*, **451**, 484
- Madau P., Dickinson M., 2014, *ARA&A*, **52**, 415
- Maseda M. V., et al., 2013, *ApJ*, **778**, L22
- Maseda M. V., et al., 2014, *ApJ*, **791**, 17
- Masters D., et al., 2014, *ApJ*, **785**, 153
- Møller P., Warren S. J., Fall S. M., Fynbo J. U., Jakobsen P., 2002, *ApJ*, **574**, 51
- Møller P., Fynbo J. P. U., Fall S. M., 2004, *A&A*, **422**, L33
- Møller P., Fynbo J. P. U., Ledoux C., Nilsson K. K., 2013, *MNRAS*, **430**, 2680
- Muzahid S., Srianand R., Bergeron J., Petitjean P., 2012, *MNRAS*, **421**, 446
- Nestor D. B., Johnson B. D., Wild V., Ménard B., Turnshek D. A., Rao S., Pettini M., 2011, *MNRAS*, **412**, 1559
- Noterdaeme P., Ledoux C., Petitjean P., Srianand R., 2008, *A&A*, **481**, 327
- Noterdaeme P., Petitjean P., Ledoux C., Srianand R., 2009, *A&A*, **505**, 1087
- Noterdaeme P., et al., 2012a, *A&A*, **540**, A63
- Noterdaeme P., et al., 2012b, *A&A*, **547**, L1
- Noterdaeme P., Petitjean P., Pâris I., Cai Z., Finley H., Ge J., Pieri M. M., York D. G., 2014, *A&A*, **566**, A24
- Noterdaeme P., Srianand R., Rahmani H., Petitjean P., Pâris I., Ledoux C., Gupta N., López S., 2015a, *A&A*, **577**, A24
- Noterdaeme P., Petitjean P., Srianand R., 2015b, *A&A*, **578**, L5
- Ocvirk P., Pichon C., Teyssier R., 2008, *MNRAS*, **390**, 1326
- Osterbrock D. E., Ferland G. J., 2006, *Astrophysics of gaseous nebulae and active galactic nuclei*
- Pâris I., et al., 2014, *A&A*, **563**, A54
- Péroux C., McMahon R. G., Storrie-Lombardi L. J., Irwin M. J., 2003, *MNRAS*, **346**, 1103
- Petitjean P., Rauch M., Carswell R. F., 1994, *A&A*, **291**, 29
- Petitjean P., Srianand R., Ledoux C., 2000, *A&A*, **364**, L26
- Petitjean P., Ledoux C., Noterdaeme P., Srianand R., 2006, *A&A*, **456**, L9
- Petitjean P., Ledoux C., Srianand R., 2008, *A&A*, **480**, 349
- Pettini M., Bowen D. V., 2001, *ApJ*, **560**, 41
- Prochaska J. X., Herbert-Fort S., Wolfe A. M., 2005, *ApJ*, **635**, 123
- Rafelski M., Neeleman M., Fumagalli M., Wolfe A. M., Prochaska J. X., 2014, *ApJ*, **782**, L29
- Rahmani H., Srianand R., Noterdaeme P., Petitjean P., 2010, *MNRAS*, **409**, L59
- Roche N., Humphrey A., Binette L., 2014, *MNRAS*, **443**, 3795
- Samui S., Srianand R., Subramanian K., 2007, *MNRAS*, **377**, 285
- Shapley A. E., Steidel C. C., Pettini M., Adelberger K. L., 2003, *ApJ*, **588**, 65
- Shibuya T., Ouchi M., Harikane Y., 2015, *ApJS*, **219**, 15
- Shull J. M., Danforth C. W., Tilton E. M., 2014, *ApJ*, **796**, 49
- Som D., Kulkarni V. P., Meiring J., York D. G., Péroux C., Khare P., Lauroesch J. T., 2013, *MNRAS*, **435**, 1469
- Songaila A., Cowie L. L., 2010, *ApJ*, **721**, 1448
- Srianand R., Petitjean P., 2000, *A&A*, **357**, 414
- Srianand R., Petitjean P., Ledoux C., Ferland G., Shaw G., 2005, *MNRAS*, **362**, 549
- Srianand R., Gupta N., Petitjean P., Noterdaeme P., Ledoux C., Salter C. J., Saikia D. J., 2012, *MNRAS*, **421**, 651
- Stanway E. R., Eldridge J. J., Greis S. M. L., Davies L. J. M., Wilkins S. M., Bremer M. N., 2014, *MNRAS*, **444**, 3466
- Stasińska G., Izotov Y., Morisset C., Guseva N., 2015, *A&A*, **576**, A83
- Steidel C. C., et al., 2014, *ApJ*, **795**, 165
- Suzuki T. L., et al., 2015, preprint, (arXiv:1505.02410)
- Trujillo I., et al., 2006, *ApJ*, **650**, 18
- Veilleux S., Cecil G., Bland-Hawthorn J., 2005, *ARA&A*, **43**, 769
- Vernet J., et al., 2011, *A&A*, **536**, A105
- Weingartner J. C., Draine B. T., 2001, *ApJS*, **134**, 263
- Wolfe A. M., Chen H.-W., 2006, *ApJ*, **652**, 981
- Wolfe A. M., Gawiser E., Prochaska J. X., 2005, *ARA&A*, **43**, 861
- Wolfe A. M., Prochaska J. X., Jorgenson R. A., Rafelski M., 2008, *ApJ*, **681**, 881
- Zafar T., Péroux C., Popping A., Milliard B., Deharveng J.-M., Frank S., 2013, *A&A*, **556**, A141
- Zanella A., et al., 2015, *Nature*, **521**, 54
- Zhu G., Ménard B., 2013, *ApJ*, **770**, 130
- Zwaan M. A., van der Hulst J. M., Briggs F. H., Verheijen M. A. W., Ryan-Weber E. V., 2005, *MNRAS*, **364**, 1467
- de Barros S., et al., 2016, *A&A*, **585**, A51

#### APPENDIX A: VOIGT PROFILE FITS TO THE METAL LINES:

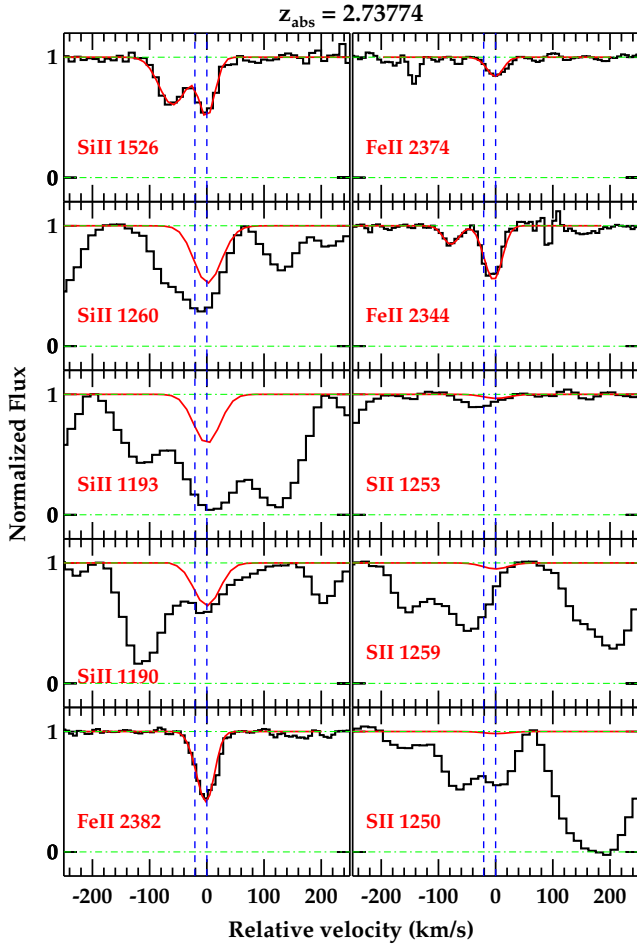


**Figure A1.** Velocity plot of low ion absorption lines detected in  $z_{\text{abs}}=2.7377$  sub-DLA together with the best fitted Voigt profiles.

**Table A1.** Voigt profile fit results for  $z_{\text{abs}}=2.7377$  system

$z_{\text{abs}}$	Species	$\log N$ ( $\text{cm}^{-2}$ )	$b$ ( $\text{km s}^{-1}$ )
2.737478	Fe II	$12.37 \pm 0.36$	$3.54 \pm 1.26$
2.737737	Fe II	$13.49 \pm 0.04$	$6.65 \pm 1.29$
	Si II	$13.90 \pm 0.14$	
	S II	$13.73 \pm 0.35$	

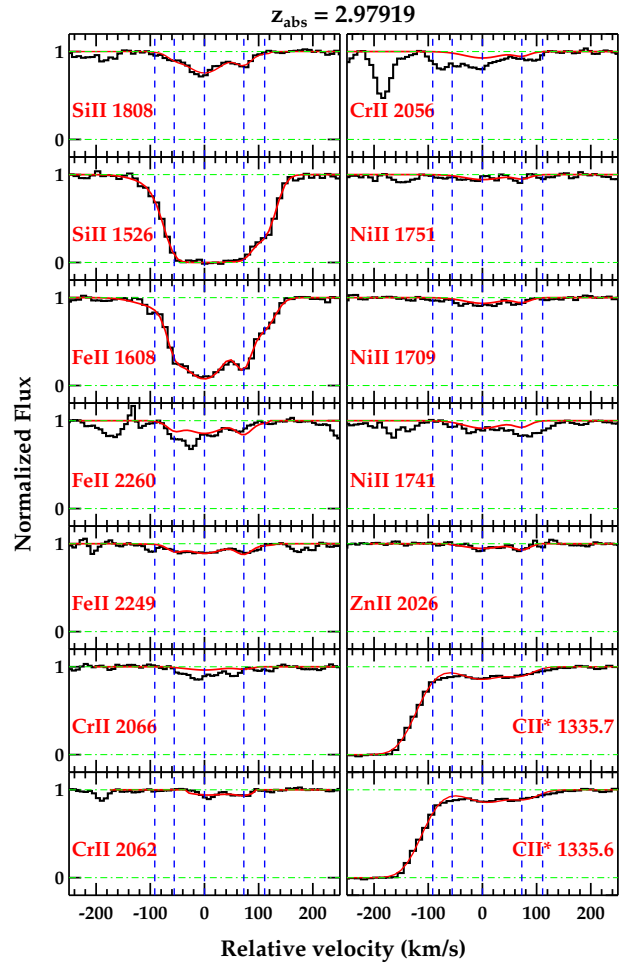


**Figure A2.** Velocity plot of low ion absorption lines detected in  $z_{\text{abs}}=2.9791$  DLA together with the best fitted Voigt profiles.

**Table A2.** Voigt profile fit results for  $z_{\text{abs}}=2.9791$  system

$z_{\text{abs}}$	Species	$\log N$ ( $\text{cm}^{-2}$ )	$b$ ( $\text{km s}^{-1}$ )
2.978455	Si II	$14.22 \pm 0.21$	$4.87 \pm 1.04$
	Fe II	$14.34 \pm 0.11$	
2.977978	Si II	$13.21 \pm 0.15$	$46.58 \pm 2.83$
	Fe II	$13.53 \pm 0.09$	
2.979195	Si II	$15.36 \pm 0.02$	$42.85 \pm 1.25$
	Fe II	$14.94 \pm 0.02$	
	Zn II	$12.23 \pm 0.08$	
	Cr II	$13.05 \pm 0.08$	
	Ni II	$13.57 \pm 0.13$	
	C II*	$13.50 \pm 0.03$	
2.980159	Si II	$14.74 \pm 0.07$	$10.05 \pm 0.93$
	Fe II	$14.61 \pm 0.06$	
	Zn II	$11.98 \pm 0.13$	
	Cr II	$12.51 \pm 0.20$	
	Ni II	$13.13 \pm 0.29$	
	C II*	$13.10 \pm 0.07$	
2.980669	Si II	$14.02 \pm 0.03$	$18.87 \pm 2.20$
	Fe II	$13.91 \pm 0.04$	

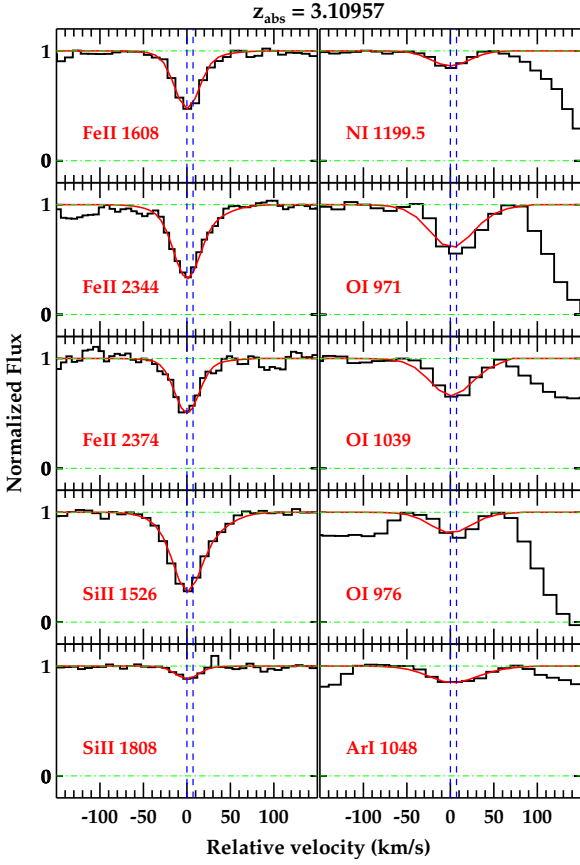


**Figure A3.** Velocity plot of low ion absorption lines detected in  $z_{\text{abs}}=3.1095$  DLA together with the best fitted Voigt profiles.

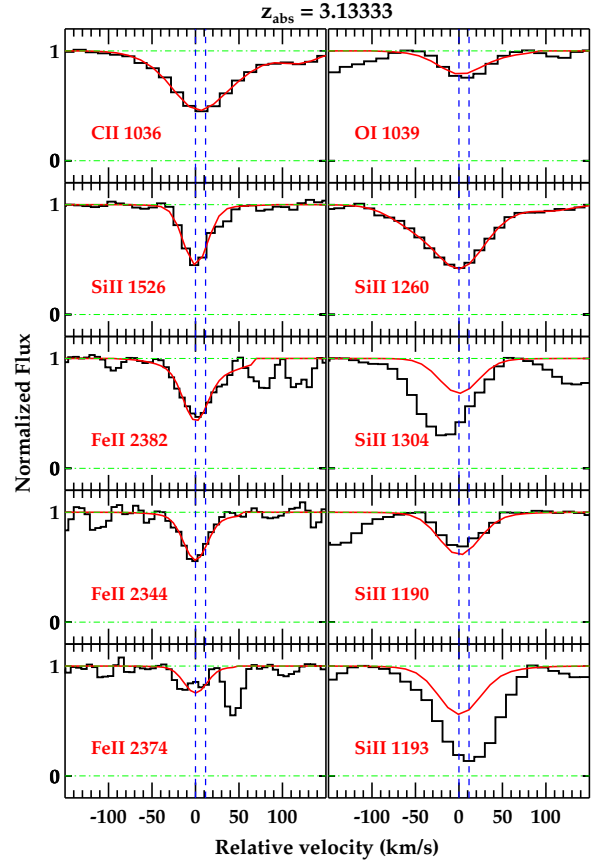


**Figure A4.** Velocity plot of low ion absorption lines detected in  $z_{\text{abs}}=3.1333$  DLA together with the best fitted Voigt profiles.

**Table A3.** Voigt profile fit results for  $z_{\text{abs}}=3.1095$  system

$z_{\text{abs}}$	Species	$\log N$ ( $\text{cm}^{-2}$ )	$b$ ( $\text{km s}^{-1}$ )
3.109576	O I	$15.18 \pm 0.12$	$6.13 \pm 0.51$
	Si II	$14.62 \pm 0.07$	
	Fe II	$14.34 \pm 0.09$	
	N I	$13.39 \pm 0.10$	
	Ar I	$12.76 \pm 0.43$	
3.109672	C II	$14.20 \pm 0.86$	
	O I	$14.55 \pm 0.13$	$37.17 \pm 2.74$
	Si II	$13.65 \pm 0.06$	
	Fe II	$13.33 \pm 0.07$	
	Ar I	$13.05 \pm 0.22$	
	C II	$14.43 \pm 0.06$	

**Table A4.** Voigt profile fit results for  $z_{\text{abs}}=3.1333$

$z_{\text{abs}}$	Species	$\log N$ ( $\text{cm}^{-2}$ )	$b$ ( $\text{km s}^{-1}$ )
3.133331	Fe II	$13.77 \pm 0.14$	$4.71 \pm 0.72$
	Si II	$14.66 \pm 0.44$	
	C II	$14.39 \pm 0.69$	
	O I	$14.70 \pm 0.21$	
3.133491	Fe II	$12.89 \pm 0.09$	$47.59 \pm 6.46$
	Si II	$12.61 \pm 0.14$	
	C II	$14.19 \pm 0.05$	
	O I	$14.55 \pm 0.16$	

**Table A5.** Voigt profile fit results for  $z_{\text{abs}}=3.2477$  system

$z_{\text{abs}}$	Species	$\log N$ ( $\text{cm}^{-2}$ )	$b$ ( $\text{km s}^{-1}$ )
3.246272	Fe II	$13.65 \pm 0.11$	$27.79 \pm 6.35$
	Si II	$13.85 \pm 0.08$	
3.247061	Fe II	$14.01 \pm 0.06$	$18.88 \pm 5.44$
	Si II	$14.33 \pm 0.07$	
3.247724	Fe II	$14.95 \pm 0.05$	$13.63 \pm 0.86$
	Si II	$15.59 \pm 0.02$	
	S II	$14.98 \pm 0.04$	
3.248624	Cr II	$13.19 \pm 0.05$	
	Ni II	$13.54 \pm 0.05$	
	Zn II	$12.47 \pm 0.06$	
	Fe II	$14.44 \pm 0.03$	$16.34 \pm 0.89$
	Si II	$14.84 \pm 0.06$	
	S II	$14.41 \pm 0.07$	
	Cr II	$12.95 \pm 0.08$	
	Ni II	$12.97 \pm 0.17$	
Zn II	$12.34 \pm 0.07$		

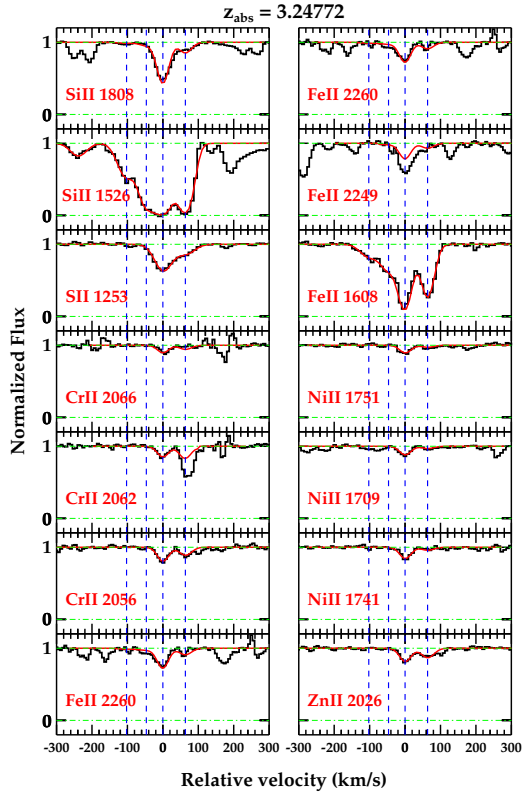


**Figure A5.** Velocity plot of low ion absorption lines detected in  $z_{\text{abs}}=3.2477$  DLA together with the best fitted Voigt profiles.